Freshwater forcing control on early-Holocene South American monsoon

Wilton Aguiar [a, *], Luciana F. Prado [b], Ilana Wainer [c], Zhengyu Liu [d], Alvaro Montenegro [d], Katrin J. Meissner [e], Mauricio M. Mata [a]

[a] Laboratório de Estudos dos Oceanos e Clima, Instituto de Oceanografia, Universidade Federal do Rio Grande - FURG, Rio Grande, RS, 96203-900, Brazil
[b] Instituto de Geociencias,Universidade de Brasilia, Campus Darcy Ribeiro, Brasilia, Distrito Federal, 70910-900, Brazil
[c] Instituto Oceanográfico da Universidade de Sao Paulo, São Paulo, 05508-120, Brazil
[d] Atmospheric Sciences Program, Department of Geography, The Ohio State University, Columbus, OH, USA
[e] Climate Change Research Center and ARC Centre of Excellence for Climate Extremes, University of New South Wales, Sydney, Australia

ABSTRACT

Climate anomalies due to Lake Agassiz outbursts and Hudson Bay ice dome melting are commonly considered triggers of North American atmospheric cooling. However, in the Southern Hemisphere, these freshwater fluxes are mostly associated with increased precipitation and a possible intensification of the South American Monsoon System (SAMS). Here, we tested how the SAMS responded to early-Holocene meltwater events. Based on both proxy data and simulations, we find that sea surface temperatures (SSTs) and precipitation indicate a freshwater-driven strengthening of the SAMS due to a weakening of the South Atlantic subtropical dipole. Simulated SAMS strengthening accounts for up to 50% of the variance in early-Holocene precipitation in South America. In turn, changes in the South Atlantic Sub-tropical Dipole accounts for up to 31% of the variance in South Atlantic SSTs. Additionally, we propose that the stronger SAMS in the early Holocene might have been due to a freshwater-driven weakening of the southeasterly trade winds. Slower trade winds weaken the zonal and meridional surface water transport, concentrating warm waters in the northeastern South Atlantic.

© 2020 Elsevier Ltd. All rights reserved.

1. Introduction

The transition from the early to the middle Holocene (11.7 ka to 4.2 ka) is characterized by the final collapse of North American ice sheets and the reorganization of the North Atlantic freshwater budget (Walker et al., 2012, 2018). An orbitally forced increase in the summer insolation is thought to have accelerated Laurentide Ice Sheet melting (Kaufman et al., 2004; Jansen et al., 2008; Bartlein et al., 2011), resulting in instability and the eventual outburst of proglacial Lakes Agassiz and Ojibway at approximately 8200 calendar years before the present (Clarke et al., 2004, 8.2 ka). Because freshwater anomalies in the North Atlantic trigger disruptions in the Atlantic meridional overturning circulation (AMOC), the large increase in lake discharges in 8.2 ka is an important component of early-Holocene climate anomalies. Widespread evidence points to diminished North Atlantic deep convection (Oppo et al., 2003; Hall et al., 2004) and AMOC weakening during the 8.2 ka event and early Holocene (Ellison et al., 2006; Kleiven et al., 2008), but uncertainties still exist regarding the propagation, intensity, timing, and spatial extent of the climate anomalies associated with the weakening of the overturning.

In the Northern Hemisphere, the 8.2 ka event is associated with widespread cold and dry conditions over North America and Europe and dry conditions over Africa and central Asia (Alley and Ágústsdóttir, 2005). Proxy data coming mostly from the northern tropical Atlantic and Western Asia indicate a decrease in the tropical precipitation associated with the 8.2 ka event (Morrill and Jacobsen, 2005). Southern Hemisphere proxy data link the 8.2 ka event to spatially heterogeneous temperature anomalies (Morrill et al., 2013) and anomaly signals in particular areas such as stronger precipitation areas over Madagascar (Voarintsoa et al., 2019) and accelerated sea-level rise and high sediment deposition rates along the Brazilian shelf (Boski et al., 2015; dos Santos-Fischer et al., 2018).

Proxy-based anomalies from South America and the South

Atlantic covering the period of interest are scarce. Multiproxy reconstructions (Morrill et al., 2013) and speleothem records (Cheng et al., 2009) associate the 8.2 ka event with increased precipitation over South America. There are indications of a sharp transition from a cooling to a warming trend centered at the 8.2 ka event in the western subtropical South Atlantic sea surface temperatures (SSTs) (Pivel et al., 2013). Like most Southern Hemisphere reconstructions, the above studies describe regional responses to the 8.2 ka event. Impacts at broader spatial scales have been connected to a strengthening of South American precipitation in speleothems and attributed to the South American monsoon system (SAMS) in the early Holocene (Cheng et al., 2009). The SAMS is one of the most important large-scale features of South America (Carvalho and Cavalcanti, 2016). In a strong SAMS regime, precipitation during austral summer increases along the Intertropical and South Atlantic Convergence Zones due to increased moisture transport (Kodama, 1992; Nieto-Ferreira and Rickenbach, 2011). The interannual variability of the SAMS is associated with the El Niño—Southern Oscillation and with the South Atlantic subtropical dipole (SASD) since those patterns induce anomalies in the wind circulation and moisture delivery to South America. (Venegas et al., 1996, 1997; Nogués-Paegle and Mo, 1997). More details on the SASD can be found in the supplementary material.

A reconstruction of the SASD has been used in conjunction with modeled precipitation to suggest an SASD-induced enhancement of the SAMS during meltwater events in the early Holocene (Wainer et al., 2014). Although the SASD signal evaluated by Wainer et al. (2014) has longer timescales than expected for the Lake Agassiz outburst, other longer-lasting freshwater fluxes in the early Holocene, such as the melting of the Hudson Bay ice dome (Gregoire et al., 2012) and rerouting of Canadian river discharge (Carlson et al., 2009), could have affected the South Atlantic in the same manner.

Here, we test the proposed relationship between the SASD, the SAMS, and precipitation over South America for the early-Holocene and evaluate the potential link between freshwater forcing from the 8.2 ka event and the SASD. Given the paucity of proxy information from the South Atlantic and South America during the period of interest, our analysis will be based on both numerical simulations and proxy data. More specifically, we plan to answer the following three questions: (1) Does the spatial pattern of reconstructed South American precipitation points to a strengthening of the SAMS around 9–8 ka? (2) Was the Early Holocene SASD shift caused by freshwater addition in the North Atlantic, i.e., a warmer northeastern South Atlantic, and if so, (3) what was the chain of mechanisms by which the increase in the freshwater discharge in the North Atlantic generated a negative trend in the SASD and strengthened the SAMS during the 8.2 ka event? This paper will be structured in the following manner to address these questions: the next section describes the proxy data, simulations and methods. Section 3 discusses the proxy-based SASD and precipitation signal. Section 4 compares the proxy data to the simulations to evaluate their ability to reproduce the SASD and South American precipitation record during the period of interest. Section 5 analyzes the temporal evolution in the AMOC and sea ice extent in the simulations. Section 6 discusses the SASD and bipolar seesaw states, and Section 7 analyzes the mechanisms of the SASD shift. Section 8 discusses the SST and wind anomalies between the AMOC slowdown and restart phases. Finally, in Section 9, we summarize the discussion and answer the questions raised in the introduction based on our results.
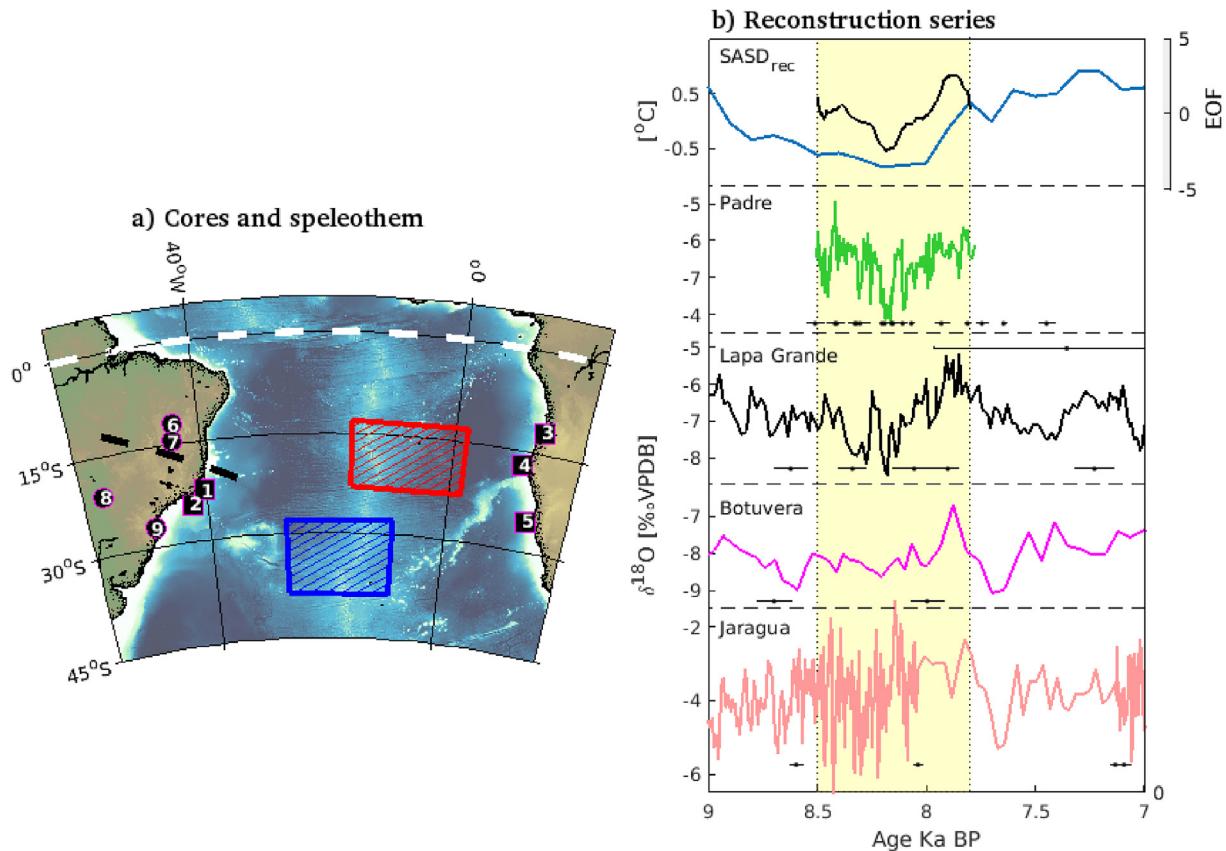
2. Data and methods

2.1. Climate reconstructions

Five SST proxy records were used to generate an early-Holocene-reconstructed SASD (Fig. 1a). The westernmost records were LaPAS-KF02 and SAN-76 located at 25°50′S 45°12′W at a depth of 827 m and 24°25′S 42°16′W at a depth of 1682 m, respectively (Toledo, 2008; Pivel et al., 2013). The easternmost cores used were ODP 1084B at 25°30′S 13°1′E and a depth of 1992 m, GeoB1023-5 at 17°9′S 11°0′E and a depth of 1978 m, and ODP 1078C at 11°55′S 13°24′E and a depth of 426 m (Kim et al., 2002, 2003; Farmer et al., 2005). The SASD$_{REC}$ index is reconstructed based on the difference in the mean SST anomalies between the eastern and western cores in an approach similar to that used in Wainer et al. (2014). The South American speleothem records include the Padre (Cheng et al., 2009) and Lapa Grande tropical caves (Stríkis et al., 2011) and the Botuverá (Bernal et al., 2016) and Jaragua subtropical caves (Novello et al., 2017). All the registers were calibrated using the most recent continental and oceanic isotopic curve based on a Monte Carlo approach.

2.2. Early Holocene CCSM3 simulations

To derive the early-Holocene SASD variability, we used one fully transient and one equilibrium simulation generated by the Community Climate System Model, version 3. The first is the simulation of the transient climate evolution over the last 21,000 years (TrACE21ka) (He, 2011). TrACE21ka has a latitude-longitude resolution of approximately 3.75°, without flux adjustments and with a dynamic global vegetation module. Starting from the initial conditions of the last glacial maximum (Otto-Bliesner et al., 2006), the simulation is forced with transient orbital parameters and greenhouse gases (Joos and Spahni, 2008), ICE-5G ice sheet reconstructions (Peltier, 2004), and meltwater forcing based on Clark and Mix (2002). To simulate early-Holocene rerouting of continental runoff, a freshwater forcing of 7.47 m/kyr in equivalent meters of sea level rise was added to Hudson Bay between 9–8 ka. Additionally, the lake outburst is simulated by adding 5 Sv (438 m/kyr) of freshwater to Hudson Bay over a time span of 6 months at 8.47 ka BP (Carlson et al., 2009; Clarke et al., 2004).

A second simulation analyzes the effect of the Lake Agassiz outburst and Hudson ice dome melting on a climate state in equilibrium, also using the Community Climate System Model, version 3. The simulation was equilibrated with the 8.5 ka orbital parameters (Berger, 1978) and greenhouse concentrations corresponding to $[CO_2] = 260\ ppm, [CH_4] = 660\ ppb$ and $[N_2O] = 260\ ppb$, with a 1° resolution. To simulate the Hudson Bay ice dome melting, a freshwater forcing of 0.13 Sv was added to the Labrador Sea within the first 99 years of simulation, while in year 1 a 2.5 Sv flux was added to simulate the lake outburst (Clarke et al., 2004). After 100 years, the simulation proceeds without any additional flux for 50 years. In contrast to TrACE21ka, this simulation compresses the 1 kyr ice dome melting to 100 years; however, previous studies show that this temporal compression of the freshwater flux does not cause significant changes in the 8.2 ka SST signal (Wagner et al., 2013; Morrill et al., 2014). In both simulations, freshwater forcing is applied to the Labrador Sea, and the 8.2 ka and early-Holocene SST and precipitation signals have been previously validated by comparison with proxy records (He, 2011; Wagner et al., 2013; Morrill et al., 2014).

Fig. 1. Speleothem $\delta^{18}O$ records for South America and the proxy-based SASD reconstructions. a) Location of the marine sediment cores (squares: 1-SAN76, 2-LaPASKF02, 3-ODP1078C, 4-GeoB10235, and 5-ODP1084B) and the speleothems (circles: 6-Padre, 7-Lapa Grande, 8-Jaragua, and 9-Botuverá). The dashed lines illustrate the locations of the Intertropical (white - -) and South Atlantic Convergence Zones (black - -), based on mean climatological position (Pottapinjara et al., 2019; Zilli et al., 2019). The red and blue boxes show the northeast and southwest SASD poles, respectively. b) The blue line at the top is the proxy-based SASD reconstruction, and the black line is the sum of the 1st and 2nd speleothem EOFs. The speleothem $\delta^{18}O$ time series are in VPDB. Age error bars for each speleothem are presented in the horizontal box plots. (For interpretation of the references to color in this figure legend, the reader is referred to the Web version of this article.)

2.3. UVic model simulation

An additional simulation was performed using the isotope-enabled University of Victoria Earth System Climate Model, version 2.9 (Brennan et al., 2012, UVic model). The UVic model is also fully coupled with ocean, land surface, atmosphere, vegetation, sea ice, and sediment components and does not include flux adjustments (Weaver et al., 2001). The model was forced with a present-day wind reanalysis by the National Center for Environmental Prediction (Kalnay et al., 1996). Time-varying geostrophic wind anomalies are computed and added to the climatology to allow dynamic feedback (Weaver et al., 2001). The Modular Ocean Model - Version 2 is the ocean component. It has 19 vertical levels with Δz varying from 50 m at the surface to 500 m at the deepest level and a resolution of 3.6^o longitude by 1.8^o latitude (Pacanowski, 1996). The model also includes sea ice (Hibler, 1979), sediment (Archer, 1996), land surface, dynamic vegetation components and fully prognostic $\delta^{18}O$ for the ocean, atmosphere, sea ice and land (Meissner et al., 2003; Brennan et al., 2012, 2013; Bagniewski et al., 2015, 2017).

The orbital parameters and carbon dioxide concentration chosen for the simulation refer to 9 ka (i.e., eccentricity = 0.0167, obliquity = 23.45^o, longitude of perihelion = 102.04^o, and $[CO_2]$ = 280 ppm) (Berger, 1978). A ten-thousand-year-long equilibrium simulation was performed to guarantee that both the ocean circulation and ocean tracers are in full equilibrium. Hence, the last 2 kyrs of the equilibrium simulation consist of the control output. The

freshwater forcing scheme is implemented from the last control year. To simulate the Laurentide Ice Sheet melting and rerouting of Canadian continental runoff, 0.086 Sv of freshwater was added to the Labrador Sea (50^oN-65^oN, 70^oW-35^oW) for one thousand years (Carlson et al., 2009, 9-8ka BP). Finally, to simulate the Lake Agassiz outburst, 2.5 Sv of freshwater forcing was added to the same Labrador Sea area in 8.5 ka (Clarke et al., 2004). In the real world, both discharges would have drained into the Hudson Bay; however, due to the rigid-lid approximation, the addition of freshwater had to be spread over a large area to avoid instabilities. After 8 ka, a virtual salt flux was added over the same region in the Labrador Sea to restart the North Atlantic deep convection. The virtual salt flux decreased from -0.2 SV to -0.05 SV between 8 and 7.5 ka. This virtual salt flux has no isotopic signature and was chosen so that the overturning could be restarted smoothly.

2.4. SASD, bipolar seesaw and wind effect analysis

The effect of the bipolar seesaw on SST anomalies was analyzed based on the first empirical orthogonal function (EOF) of the Atlantic SSTs. Since the surface signal of the bipolar seesaw is directly affected by the strength of the AMOC overturning (Pedro et al., 2018), an AMOC index, i.e., the maximum overturning streamfunction between 20^oN-70^oN and between 200 and 3000 m, was calculated as in (Yang et al., 2015). The total sea ice area was also calculated for the models due to its effect on global SST patterns and deep water formation (Chiang and Bitz, 2005). To analyze

the SASD variability in the early Holocene, we calculated the model-based SASD index in two ways. First, the SASDMODEL area index was obtained by calculating the difference in the SST anomalies between the southwest (30°-40^oS, 30°-10^oW) and northeast (15°-25^oS, 0°-20^oW) areas of the dipole region (Morioka et al., 2011). Hence, SASDMODEL measures the rate of warming (or cooling) between the South Atlantic poles, with a negative SASDMODEL meaning stronger warming in the northeast South Atlantic or stronger cooling in the southwest South Atlantic, and vice versa (Lorenz, 1956; Morioka et al., 2011, Figure C3). Since the core-based SASDREC is the difference between coastal temperatures, we calculated SASDCOAST, which takes the difference in SST anomalies at the coastal cells of each model within the latitude range of each pole of the SASDMODEL index. SASDMODEL is calculated following the definition of the SASD index by Morioka et al. (2011), but the addition of SASDCOAST assures comparability with SASDREC.

Vertical displacement of the thermocline along longitudes can be triggered by either wind action or horizontal water mass advection into the South Atlantic. Specifically, shifts in the meridional component of the winds change the zonal surface Ekman transport and rearrange the zonal SST distribution. Using the 1.5 layer model and Ekman dynamics, we are able to derive how changes in the trade winds affect the thermocline depth (Eq. (1)).

$$h^2(x,y) = \frac{2f^2(y)}{\beta(y)\gamma}w_e(x - x_e) + H^2(y) \tag{1}$$

where $h(x,y)$ is the predicted isothermal depth as a function of the longitude (x) and latitude (y). $H(y)$ is the depth of the chosen isotherm in the eastern boundary, and $D(x,y) = \sqrt{\frac{2f(y)^2}{\beta(y)\gamma}w_e(x - x_e)}$ is the increment of the isothermal depth over the basin. The variables $(x - x_e)$, w_e and $\gamma = \frac{\rho_3 - \rho_2}{\rho_0}g$ are the distance from the eastern boundary, Ekman pumping and density stratification, respectively. The values chosen for ρ_2 (1025 kg m^{-3}) and ρ_3 (1035 kg m^{-3}) represent the approximate mean densities above and below the thermocline, respectively. $\rho_0 = 1020$ kg m^{-3} is a reference density. Finally, $f(y)$ is the Coriolis parameter, and $\beta(y)$ is the beta effect parameter. The parameter that tracks the vertical displacement of the isotherms along the longitudes ($D(x,y)$) depends on Ekman pumping changes. Hence, $h(x,y)$ measures how wind changes affect a specific isotherm. Although the 20^oC isotherm is traditionally used to track thermocline depth, this isotherm emerges north of 35^oS in both simulations, i.e., north of the maximum latitudinal extent of the SASD. We therefore chose to track the 17^oC isotherm, which lies close to the top of the thermocline. The full derivation of Eq. (1) is found in the supplementary material. Finally, wind patterns also respond to sea ice alterations. Sea ice expansion may intensify trade winds (Chiang and Bitz, 2005). As sea ice changes influence Antarctic Bottom Water and North Atlantic Deep Water formation, we also analyze simulated sea ice areas (SIAs).

3. Precipitation and SASD records

First, we analyzed the SASD and SAMS signals in ocean cores and precipitation. The reconstructed SASDREC index shows a decrease in the dipole between 9 and 8 ka by up to 1^oC, followed by an increase after 8 ka (Fig. 1). A negative SASD index is associated with anomalous warming of the northeast South Atlantic, which in turn enhances the SAMS by increased evaporation (Liebmann and Mechoso, 2011). Precipitation over South America is mediated by convergence and convection over the ITCZ and SACZ (Garcia and Kayano, 2010; Souza and Cavalcanti, 2009). However, intensified evaporation in the northeast South Atlantic during negative SASD
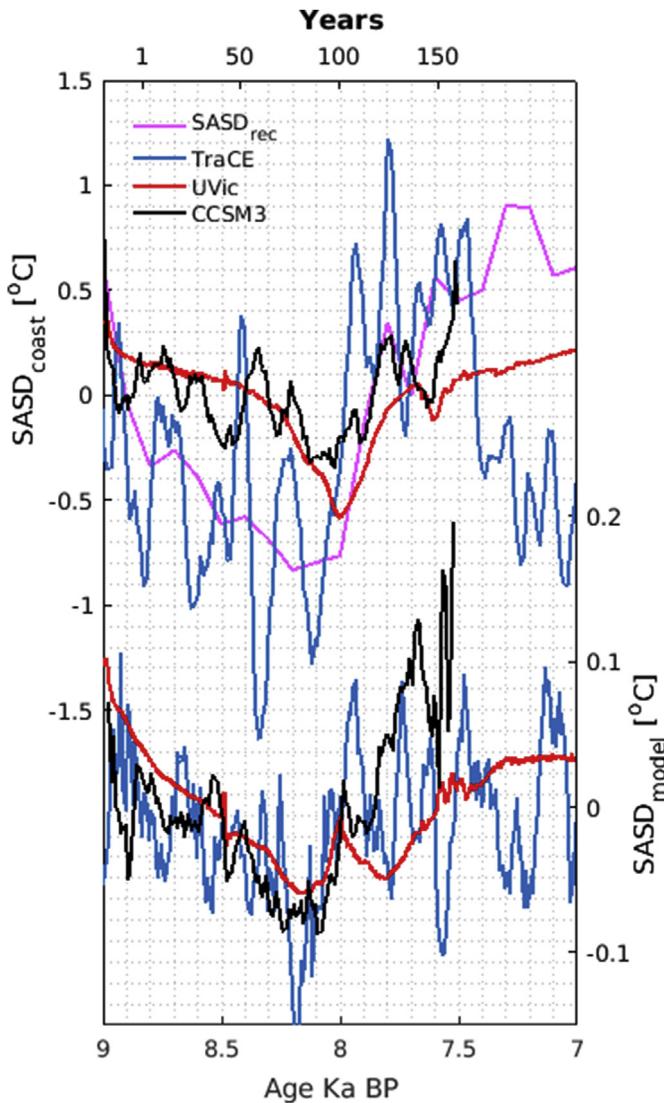
events enhances water vapor saturation over the convection bands, strengthening the precipitation (Monerie et al., 2019; Wainer et al., 2014). The spatial footprint of a strong SAMS is an increment in the precipitation along northeast South America (Vera et al., 2006), with this increment decreasing from the north towards southernmost South America (Fig C3 - supplementary). Speleothem $\delta^{18}O_p$ records along South America can help us determine if, in fact, an increase in the precipitation signal is recorded between $9-8$ ka. Lapa Grande and Padre speleothem reconstructions register a decrease in $\delta^{18}O_p$ from $9-8.2$ ka, pointing to an increase in precipitation in this period (Fig. 1). In both caves, $\delta^{18}O_p$ increases after 8.2 ka, pointing to a decrease in precipitation. Conversely, an SASD negative event decreases the SST over the southwestern South Atlantic. This decrease in SST counter-balances the stronger evaporation in the northeast South Atlantic, which then causes the precipitation signal to decrease southwards (Liebmann and Mechoso, 2011). Jaragua Cave is located south of the previous speleothems. As expected for southern South America, there is a minimal $\delta^{18}O_p$ decrease between $8.5-8.3$ ka and an increase after 8.3 ka. Botuverá cave is the southernmost speleothem considered in this study. Since the SAMS has a lowering effect on southern South America precipitation, if the recorded changes in the precipitation are due to changes in the SAMS, we would expect very small or no precipitation variation in this record. In fact, the Botuverá speleothem shows no significant changes in $\delta^{18}O_p$ except for a slight increase (precipitation decrease) between 8.2 ka and 7.9 ka. The decrease in the precipitation variation from northeastern to southern South America is an indication of SAMS-driven precipitation events. Notice also that the SASDREC index is correlated with $\delta^{18}O_p$ changes recorded in the caves, implying the influence of the SASD pattern on the SAMS.

EOF analysis was performed for the Padre, Lapa Grande, Botuverá and Jaguara Caves within their maximum gap-free time range (8.5 ka - 7.8 ka, the yellow band in Fig. 1b). The sum of the first and second components show a decrease in $\delta^{18}O_p$ from $8.5-8.2$ ka and explains 89% of the total speleothem record variability (Fig. 1b - top). The maximum cross-correlation of the sum of the EOFs with the reconstructed SASD equals 0.83 (nPREC = 231,unfiltered), with an SASD lag of 21 years, which indicates the coevolution of those patterns. Although this lag is large considering the real world SST-precipitation coupling, one has to bear in mind that the dating error for the marine records used here is up to 60 years (Pivel et al., 2013). Still, the 21 years lag is in agreement with the time scale of the response of the global monsoons to a change in the South Atlantic meridional heat transport estimated by Lopez et al. (2016).

The synchronous signal in the reconstructed SASD and speleothem $\delta^{18}O_p$ hints that the change in precipitation in the early Holocene is tied to the recorded change in the SASD. Moreover, due to the scarcity of early-Holocene precipitation and SST reconstructions, climate model simulations can be a helpful tool to further explore the connection between the SASD and SAMS.

4. Simulated SASD signal

Prior to analyzing the early-Holocene simulations, it is necessary to test whether they reproduce the SASD and precipitation signals described in Section 3. We therefore compare SASDREC with the simulated SASDCOAST value and the speleothem $\delta^{18}O_p$ with the simulated precipitation. SASDREC is created by taking the difference in the SST anomalies between records in the coastal cores. Because the coastal gradients may differ from open-ocean ones, we calculated the difference between the SST anomalies off the African and Brazilian coasts at the latitudes of the northeast and southwest poles (Section 2.4, SASDCOAST). The SASDCOAST values in TrACE and UVic decrease by 1.5^oC and 1^oC, respectively, from 9 to 8 ka (Fig. 2 -

Fig. 2. $SASD_{REC}$, $SASD_{COAST}$ and $SASD_{MODEL}$ time series. The UVic and TrACE integration years are shown on the bottom x-axis, while the CCSM3 integration years are shown on the top x-axis. The $SASD_{COAST}$ and $SASD_{MODEL}$ values are on the left and right y-axes, respectively.

top). After 8 ka, the $SASD_{COAST}$ values in both simulations increase back to its initial value. The UVic and TrACE long-term behaviors are very similar to $SASD_{REC}$ for the period, having a similar magnitude of $1.5^{o}C$. It must be stressed, however, that after 7.5 ka, the TrACE $SASD_{COAST}$ decreases again, unlike $SASD_{REC}$. The CCSM3 simulation is forced with a freshwater flux over the first hundred years of the experiment, leading to a decrease in $SASD_{COAST}$ over this period of time. The coastal index then recovers within 50 years after the freshwater forcing ends. Hence, all the models reproduce the magnitude and trends in the SASD changes in the proxy records.
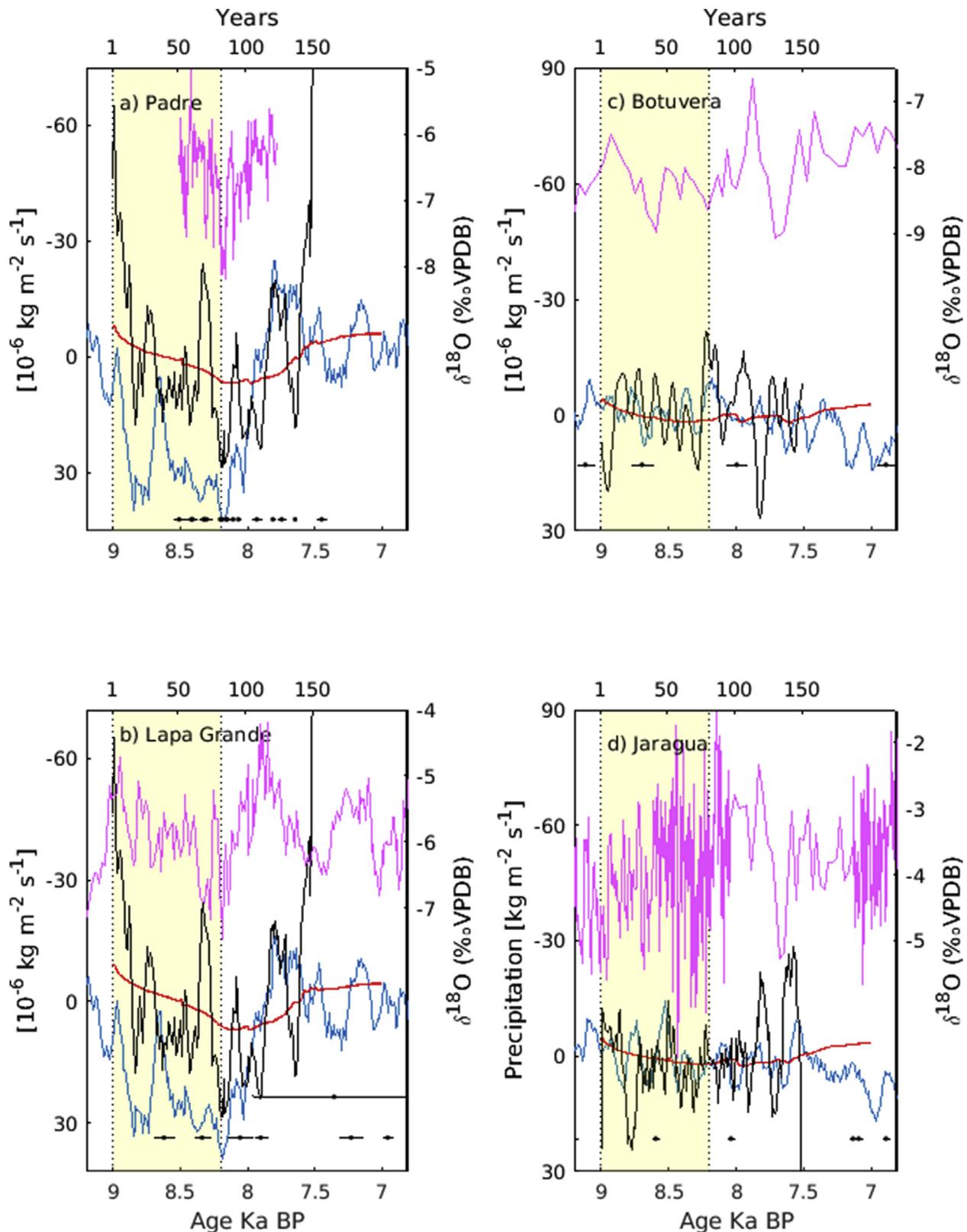
Comparing $SASD_{COAST}$ with $SASD_{MODEL}$, we can see that the coastal index does reproduce the main decreasing trend between 9 and 8 ka as well as the posterior increase in $SASD_{MODEL}$. The smaller range in the variation in $SASD_{MODEL}$ (approximately $0.2^{o}C$) is due to SST anomalies being calculated based on the area means, resulting in lower variability. Even though the range of variability in $SASD_{MODEL}$ seems small, full SASD events have been identified to have SST anomalies of up to $0.6^{o}C$ (Nnamchi et al., 2017), and hence a 0.2 ^{o}C shift would induce higher frequency and persistence of negative

SASD phases. The similarity between signals indicates that the $SASD_{MODEL}$ index captures the main variability in the proxy SASD.
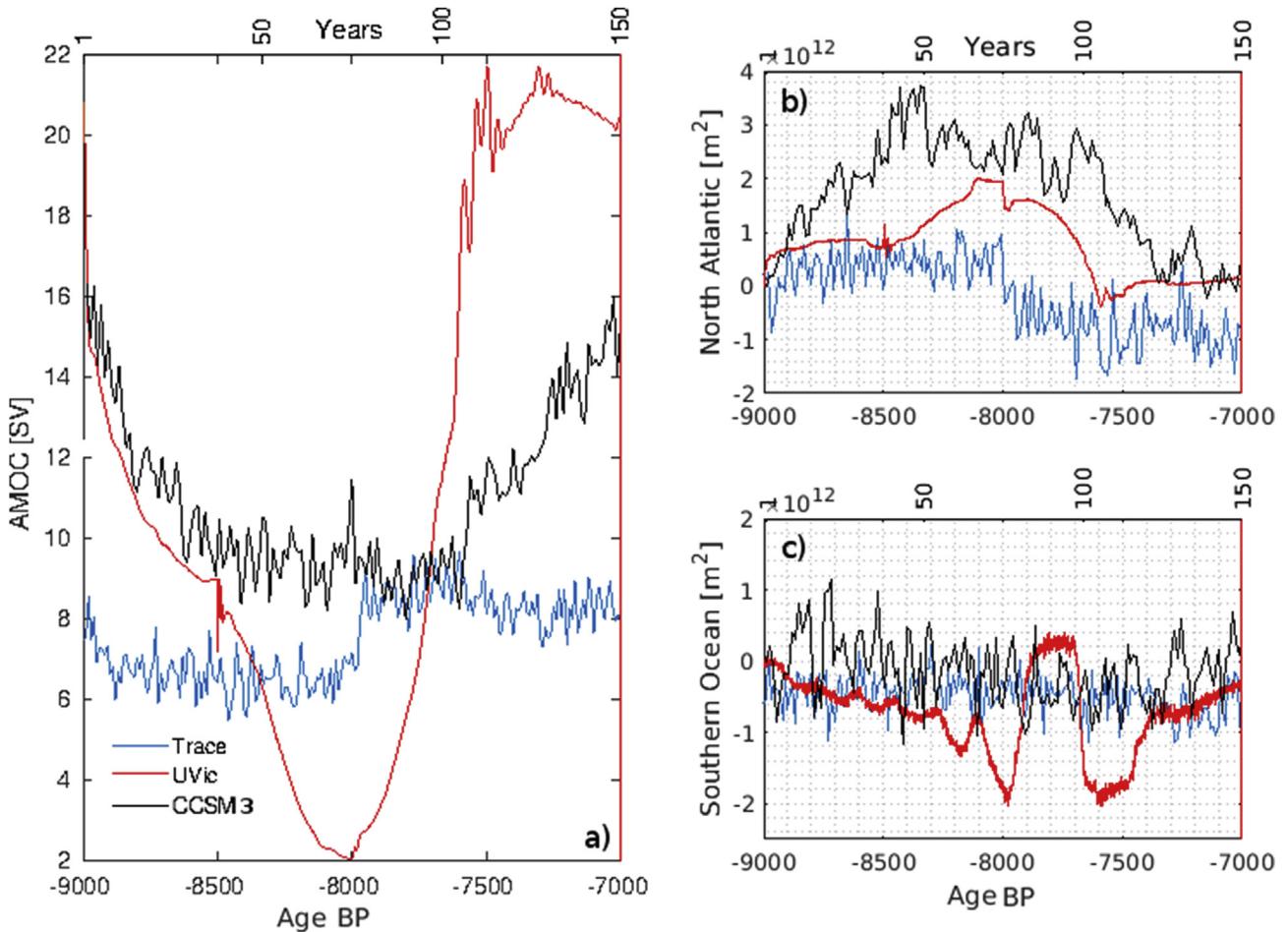
We also compared the simulated precipitation at each cave location to the speleothem oxygen isotope ratio. The simulated precipitation increases at both the Padre and Lapa Grande Caves from 9−8 ka in the TrACE and UVic simulations and within 1−100 years in CCSM3 (Fig. 3a and b). As the amount of precipitation increases, $\delta^{18}O_p$ decreases, and this signal is present in the $SASD_{MODEL}$ index. The TrACE, CCSM3 and UVic precipitation amounts increase by approximately 3×10^{-3}, 9×10^{-5} and 1×10^{-5} kg m^{-2} s^{-1}, respectively. The mean model-calculated precipitation at the cave locations ranges from 3.8×10^{-5} kg m^{-2} s^{-1} to 4.5×10^{-5} kg m^{-2} s^{-1}, so the anomalies represent a considerable precipitation increase. After freshwater forcing ends (8 ka and 100 years), precipitation decreases again while the $\delta^{18}O_p$ increases. The simulated precipitation in the southernmost caves (Jaragua and Botuverá) does not show a clear trend, agreeing with the lack of trend in $\delta^{18}O_p$. When taking into account both the simulated SASD and precipitation signal, all three simulations show a decreasing signal from 9 to 8 ka (increasing precipitation) and a rise afterward. This is the signal we are interested in analyzing and thus we can have more confidence in using the models to study the dynamical processes leading to reversed SASD and strengthened SAMS in the early Holocene.

5. Simulated overturning

Climate reconstructions and simulations have shown that freshwater added to the North Atlantic has the potential to concentrate heat in the South Atlantic and weaken the Southern Hemisphere trade winds by weakening interhemispheric transport (Chiang and Bitz, 2005; Chiang et al., 2008; Kim et al., 2002; Pedro et al., 2018). Changes in both the heat transport and trade wind shifts impact sea surface temperature patterns in the South Atlantic (Stocker et al., 1992; Wagner, 1996) and hence affect the SASD. Overturning in the TrACE simulation decreases from 8 Sv to approximately 6 Sv between 9 and 8 ka and recovers after 8 ka, reaching 9 Sv (Fig. 4a). Note that the freshwater addition timing in TrACE is concurrent with the AMOC weakening between 9 and 8 ka. During the slowdown phase of the AMOC, the circulation weakens by 1.5 Sv, but the main structure of the circulation does not change (Fig C4-a). The weakening is noticeable in the upper 2000 m. As AMOC weakens, zonal velocities decrease in the location of the northeastern SASD pole (Fig C4-c). After the freshwater forcing stops (8−7 ka) the AMOC recovers with an intensification of the circulation and a deepening of NADW (Fig C4-b 1000−3000m), and zonal velocities are restored to the 9.1 ka values (Fig C4-d). The CCSM3 non-transient simulation (CCSM3 hereafter) has a duration of 150 years and starts with the Lake Agassiz outburst. The CCSM3 overturning is similar to TrACE: the AMOC in this simulation drops from 16 Sv to 9 Sv within the first 100 years of freshwater forcing. After year 100, when freshwater forcing stops, the AMOC recovers, reaching approximately 15 Sv by the end of the 150 years of simulation. The AMOC in the UVic simulation weakens from approximately 20 Sv−2 Sv during the freshwater forcing period (9−8 ka). After 8 ka, the AMOC restarts and stabilizes to approximately 20 Sv again by 7.5 ka. TrACE is fully transient and accounts for the freshwater forcing discharges associated with Heinrich event 1 and the Younger Dryas prior to the Holocene (He, 2011). The forcing prior to the Holocene possibly diminishes initial overturning in TrACE, making the initial AMOC overturning lower than that of CCSM3. Considering that the total mass added to the ocean in TrACE (7.5 m in SLR equivalent) is larger than in CCSM3 (1.5 m in SLR equivalent) and that both TrACE and CCSM3 use the Community Climate System Model, version 3, we can infer that the stronger

Fig. 3. Comparison between the simulated precipitation and $\delta^{18}O_p$ for South American caves. Blue, red and black lines are the TrACE, UVic and CCSM3 precipitation time series at the cave locations, respectively. The purple line is the cave $\delta^{18}O_p$. The UVic and TrACE integration years are shown on the bottom x-axis, while the CCSM3 integration years are shown on the top x-axis. The yellow band marks the period of decreasing SASD. Note that the precipitation vertical axis is flipped, with values decreasing from top to bottom. The right y-axis in all plots are for the $\delta^{18}O_p$ series, while the left y-axis are for the simulated precipitation. (For interpretation of the references to color in this figure legend, the reader is referred to the Web version of this article.)

Fig. 4. AMOC index [Sv] for all the simulations (a) and sea ice extent anomalies [$10^{12}m^2$] in the North Atlantic (b) and Southern Ocean (c). The blue and red curves correspond to the TrACE and UVic simulations, respectively, and the time integration is shown on the bottom horizontal axis, while the black curve corresponds to CCSM3, and the integration time is shown on the top horizontal axis. (For interpretation of the references to color in this figure legend, the reader is referred to the Web version of this article.)

decrease in AMOC in the CCSM3 simulation is possibly due to higher freshwater flux over a shorter time. In turn, the stronger AMOC slowdown in the UVic simulation compared to TrACE is possibly due to the stronger sensitivity of the UVic model to hosing. All models show a weakening of the overturning that reaches a minimum by the end of the respective freshwater addition, and after hosing ends, AMOC recovery takes place.

The zonal heat distribution in the Atlantic is directly affected by zonal Ekman transport, which in turn responds to wind shifts. Moreover, sea ice expansion can have an impact on trade winds and deep water formation (Chiang and Bitz, 2005). Fig. 4b shows the total sea ice area in the Northern Hemisphere for all simulations. In all three simulations, the North Atlantic sea ice area (SIA) increases during the freshwater forcing period, i.e., approximately 9–8 ka for TrACE and UVic and 1–100 years for CCSM3. The TrACE and UVic SIAs increase by approximately $1 \times 10^{12}m^2$ and $2 \times 10^{12}m^2$, respectively, while the CCSM3 area increases by $3 \times 10^{12}m^2$. At 8 ka, with the AMOC restart, heat transport is restored in the North Atlantic, and the SIA starts to decrease again in the UVic and TrACE experiments. After 7.5 ka, the North Atlantic SIA plateaus into a new equilibrium value as the AMOC reaches equilibrium as well. In CCSM3, the SIA reaches its maximum after approximately 50 years of simulation, stays relatively high until year 80 and decreases afterward. Despite the distinct variability in each simulation, the time series of the AMOC index and the North Atlantic SIA have a

coherent pattern: As freshwater is added to the North Atlantic (9–8 ka or 1–100 years), the AMOC slows down and sea ice expands in the North Atlantic, while the opposite occurs when freshwater forcing stops.

The Southern Ocean SIA response to AMOC changes varies between models (Fig. 4c). While both the TrACE and CCSM3 exhibit no significant Southern Ocean sea ice response to the freshwater forcing in the early Holocene, the UVic model shows high SIA variability. From 9 to 8 ka, the UVic SIA decreases by $2 \times 10^{12}m^2$ in the Southern Ocean. This decrease is triggered by an increase in open-ocean deep convection and Antarctic Bottom Water formation, melting sea ice due to warmer water advected southward and brought up from deeper layers in the Southern Ocean (supplementary materials). This behavior is consistent with the bipolar seesaw hypothesis (Broecker, 1998). From 8 ka-7.5 ka onwards, strong positive anomalies in the SIA occur, as Antarctic Bottom Water formation reaches its maximum (see Fig B2-3 in the supplementary materials). Finally, after 7.5 ka, the AMOC stabilizes, and as the Southern Ocean starts to cool down again, the SIA increases, which is an ocean dynamic response to North Atlantic overturning slowdown. Southern Ocean deep convection events in the open ocean in the UVic model have been previously described by Meissner et al. (2007). Similar processes have been suggested by Azaneu et al. (2014) and Aguiar et al. (2017) for reanalysis products. This 8–7.5 ka signal does affect the SASD (Section 6), and we will

analyze the SASD anomalies in this period. However, those anomalies are outside the period that we aim to analyze for the freshwater forcing response (9−8 ka) and are therefore not the focus of this study.
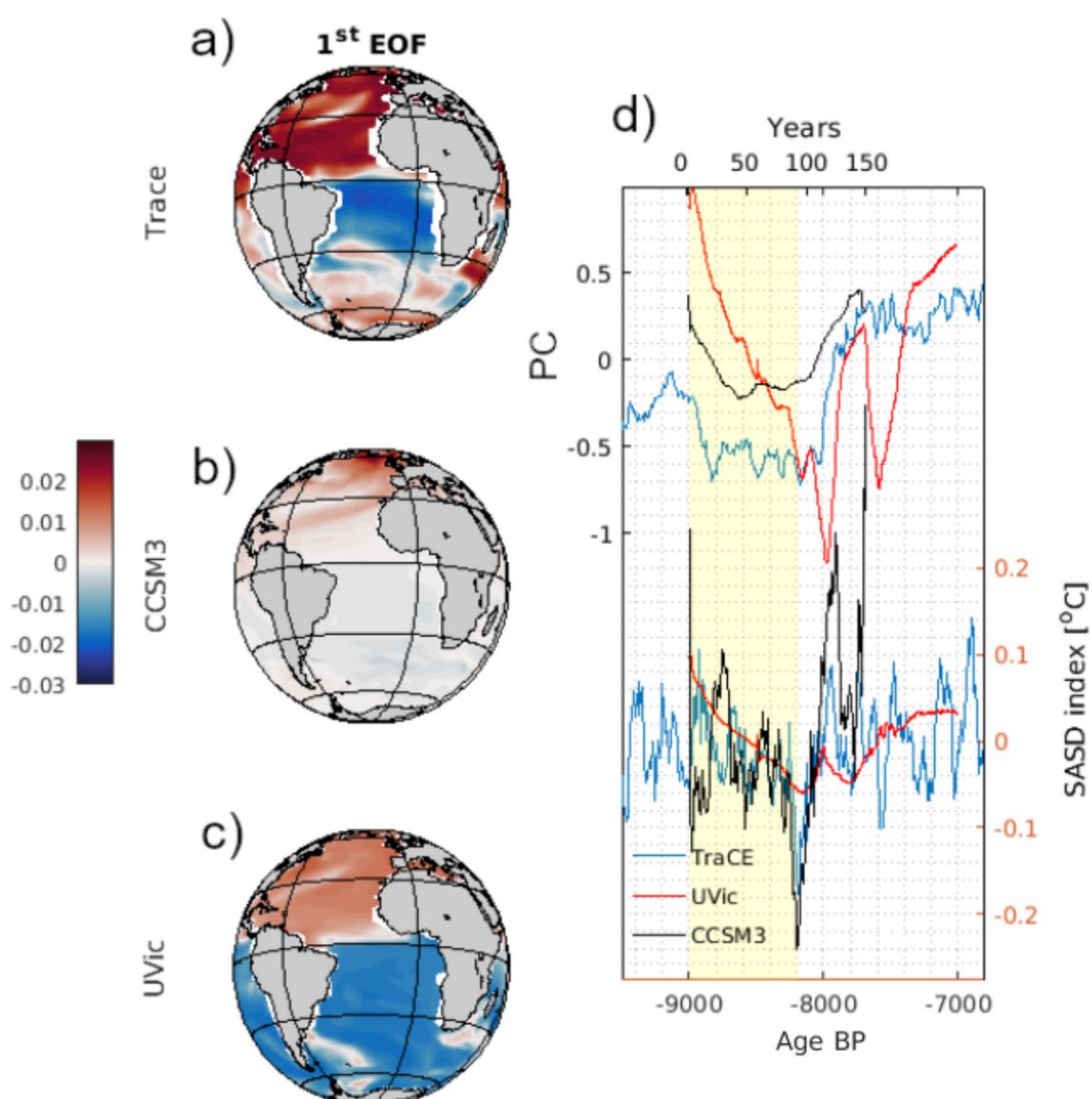
6. Early-holocene SASD

EOF analysis was performed to determine the main variability pattern in all the simulated SSTs and their link with the SASD between 9−7 ka (Fig. 5). The first global components of the SST EOF analysis have correlations of 0.72, 0.6 and 0.87 with the AMOC index for TrACE, the UVic model and CCSM3, respectively. The spatial pattern of the first EOF shows positive temperature anomalies in the North Atlantic and negative ones in the South Atlantic (Fig. 5a−c). When the AMOC weakens (9−8.2 ka and 1−100 years), the 1st component from all the models show warming in the South Atlantic and cooling in the North Atlantic.

After freshwater forcing stops, the time series of the first EOF

from both TrACE and CCSM3 increase, restoring the North and South Atlantic SSTs. In the UVic simulation, the 1st component also increases after the cessation of freshwater forcing but has an oscillatory behavior between 8 and 7.6 ka. This oscillation matches the variability in the Southern Ocean deep convection and sea ice area discussed above (Fig. 4c).

In all three models, as the AMOC weakens and the South Atlantic warms, the area-based SASD index moves towards negative values (Figs. 5d, 9−8.2ka). The decrease in the SST gradient equals 0.3^{o}C, 0.4^{o}C, and 0.2^{o}C in the TrACE, CCSM3 and UVic simulations, respectively. As the AMOC restarts, the SASD$_{MODEL}$ indices for the TrACE, CCSM3 and UVic simulations increase towards positive values again. The SASD$_{MODEL}$ index in the UVic simulation again shows an oscillation due to changes in AABW formation. This oscillation is a quarter of the magnitude (0.05^{o}C) of the main SASD decay (0.2^{o}C); hence, we consider it a minor departure from the main SASD$_{MODEL}$ increase.

A negative SASD$_{MODEL}$ value is therefore a consistent response to

Fig. 5. EOF analysis of the sea surface temperature and SASD$_{MODEL}$. Maps a, b and c represent the 1st EOF components for the globe in TrACE, CCSM3 and UVic simulations, respectively. Graph d is the time series of the normalized values for the 1st component (top) and nonnormalized area-based index (SASD$_{MODEL}$ - bottom). The yellow box highlights the period of slowing AMOC in all simulations. (For interpretation of the references to color in this figure legend, the reader is referred to the Web version of this article.)
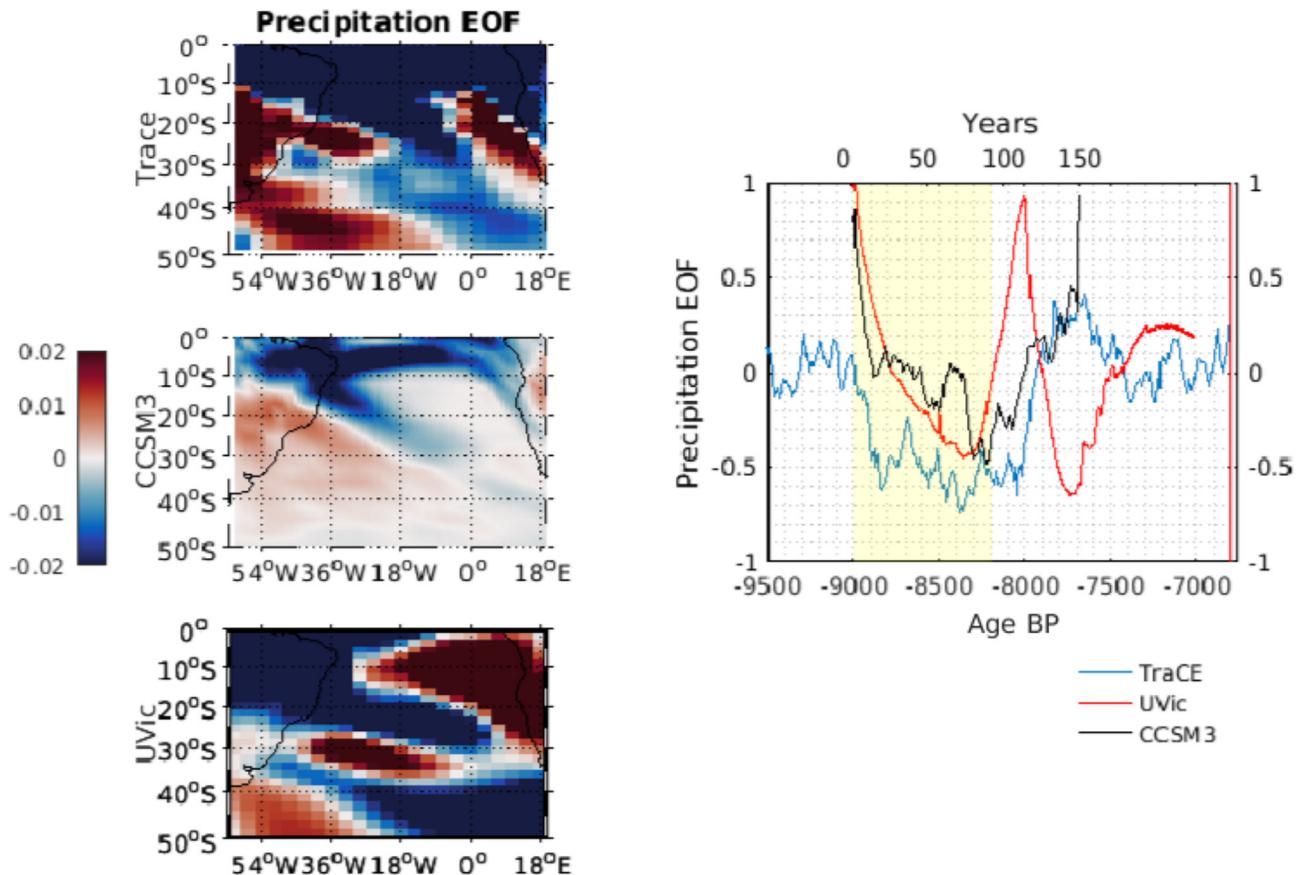
freshwater anomalies between 9 and 8 ka. The agreement between the simulations and reconstructions (SASD_REC, Fig. 2) points to the persistence of a weaker dipole in the transition from the early to middle Holocene. After the freshwater addition period ends, the SASD values increase again. Since the simulations forced only with meltwater (CCSM3 and UVic model) show a decrease in the SASD, the freshwater addition to the North Atlantic, and not the other transient forcings included in the TrACE simulation, is likely the forcing responsible for triggering the SASD shift in the early Holocene.

Negative SASD events enhance the SAMS by increasing the amount of precipitation over the ITCZ and SACZ (Liebmann et al., 2004), with increased precipitation over northeastern South America and decreased precipitation in southern South America (Cavalcanti, 2012). The SST-precipitation coupling mechanism proposed by Wainer et al. (2014) states that warming over the northeast SASD pole during a negative SASD phase enhances ocean evaporation, resulting in higher atmospheric moisture over the respective latitudinal band. An EOF analysis of the precipitation was performed here to evaluate the evolution of the precipitation pattern. The components that captured the SAMS spatial signal were the 1st EOF for the TrACE and CCSM3 simulations and the 2nd EOF for the UVic simulation, showing anomalies in the Intertropical and the South Atlantic Convergence Zones (Fig. 6). A positive EOF signal for the three simulations represents negative precipitation anomalies over the SACZ and ITCZ, and a shift towards positive anomalies southwards. The three simulations are characterized by

a shift of the EOF time series towards negative values when the AMOC is weakened; i.e., the precipitation increases in northeastern South America (Fig. 6d). When the AMOC recovers, the TrACE and CCSM3 principal components increase back to their initial values. During recovery, the UVic simulation shows the oscillation already described in the SST and sea ice signals, which points to an SST-precipitation coupling in the mechanism. The EOFs describing the SAMS variability explain 51%, 50% and 30% of precipitation variability in TrACE, CCSM3 and UVic experiments, respectively. Finally, the synchronous weakening of the bipolar seesaw and precipitation EOFs and SASD index during overturning slowdown suggests that there is a link between the AMOC strength, SASD negative and SAMS positive anomalies. A Pearson's correlation between the SASD_MODEL and the precipitation principal component time series results in correlation coefficients of 0.62, 0.70, and 0.46 for TrACE, CCSM3, and the UVic model respectively ($p < 0.05$), showing a moderate relationship between the patterns. Moreover, the determination coefficients from a linear regression between the SASD-MODEL and precipitation are 0.38, 0.5, and 0.21 in TrACE, CCSM3, and UVic simulations, respectively. Those determination coefficients suggest that SASD explained up to 50% of the precipitation signal of SAMS during the 8.2 ka event. Hence the SASD possibly exerts a second-order forcing on the precipitation in the early-Holocene.

7. Mechanisms of SASD variability

The zonal heat distribution in the South Atlantic is directly

Fig. 6. SAMS signal of the precipitation in the EOF analysis. The maps represent the precipitation EOF component for the South Atlantic and South America in the simulations. The graph is the time series of the values for the principal components of the EOFs. The yellow box highlights the period of weaker AMOC in all simulations. The precipitation modes in the TrACE, CCSM3 and UVic simulations explain 51%, 50% and 30% of the precipitation variability, respectively. (For interpretation of the references to color in this figure legend, the reader is referred to the Web version of this article.)
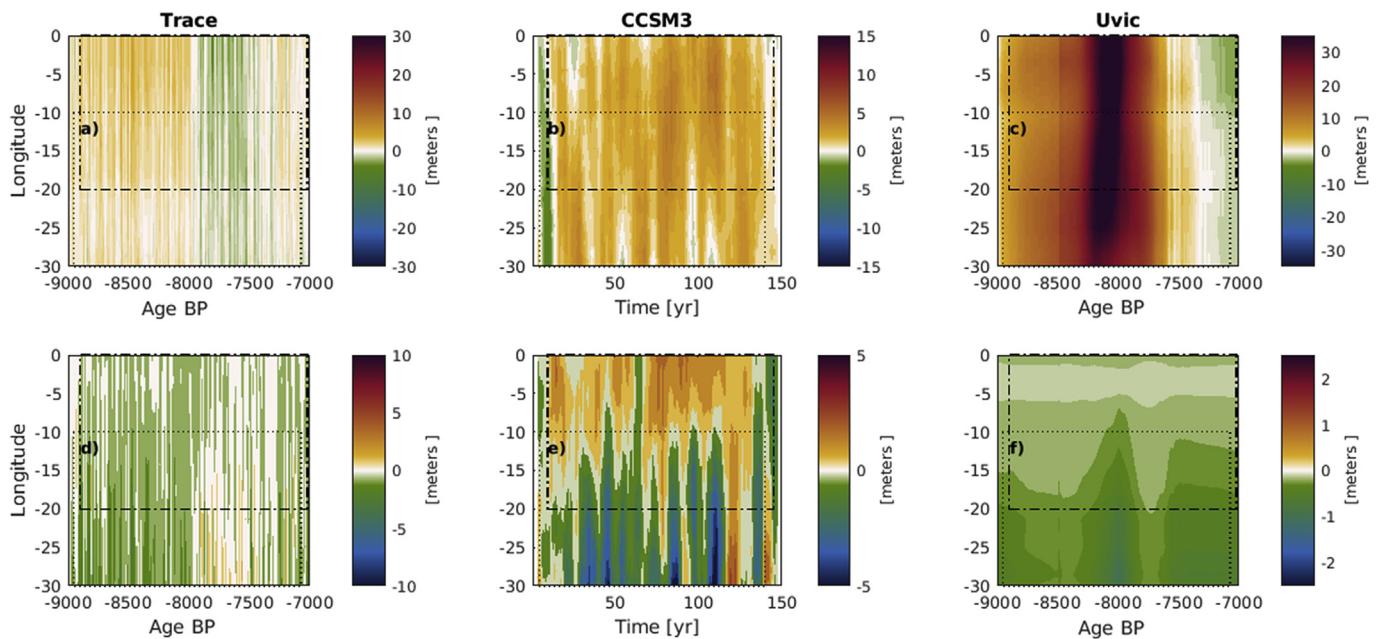
affected by the strength of the trade winds. A weaker wind meridional component decreases the westward Ekman transport, displaces the surface heat from the Brazilian coast towards the African coast, and reduces the depth of the thermocline. Hence, changes in the wind during the early Holocene could have altered the surface mixed layer heat content in the SASD poles, shifting the system. To analyze the role of the winds in shifting the SASD towards negative values, we used the 1.5 layer solution (Eq. (1)) to compute the depth of the $17^{o}C$ isotherm. In TrACE, the wind causes a shallowing of the $17^{o}C$ isotherm within the South Atlantic during 9−8 ka, i.e., during freshwater forcing, with an upward displacement of up to 3 m (Fig. 7d), which is larger in the western Atlantic. In the CCSM3 experiment, the wind-induced shallowing of the western isotherms of 10 m and a 5 m deepening of the eastern isotherm (Fig. 7e) from year 1−100. The same pattern is observed in the UVic simulation from 9−8 ka, with a maximum shallowing of a meter (Fig. 7f), especially after 8.5 ka. The wind anomalies in the UVic simulation derive from a geostrophic adjustment to air temperature anomalies, and not from a fully resolved atmospheric dynamics. This method of adjustment might explain the low magnitudes of isothermal deepening in the UVic simulation. Nevertheless, the upward movement of the thermocline indicates cooling of surface waters by their mixing with deep colder waters. Accordingly, as western isotherms move upwards, it is expected that colder deep waters will reach the surface, cooling the SST distribution of the southwestern SASD pole, and pushing the dipole towards negative values. The simulated decay of the SASD from 9−8 ka in Fig. 5d hints this is the process responsible for shifting the SASD. Hence, when freshwater is added to the North Atlantic, winds tilt the isotherms, which results in the development of a negative SASD phase.

After the freshwater forcing period, TrACE winds push the isotherms down again in the western South Atlantic, pushing the dipole index towards the positive phase (Figs. 7d, 8-7ka). In CCSM3, the wind-driven isothermal downlift occurs after year 110 (Fig. 7b). The western isotherms deepen by up to 5 m after year 110, and the eastern Atlantic isotherms move upwards from 130 to 150 years in CCSM3. This motion drives the dipole towards positive values by

cooling the notheastern SASD pole and warming the southwestern pole. In the UVic model, wind-driven isothermal downlift occurs through an oscillation (Fig. 7f). First, the western Atlantic isothermal depth anomaly becomes less negative, i.e., western isotherms move downwards from 8.2−7.8 ka. This motion pushes the dipole towards positive values (Fig. 5d) by warming the southwestern SASD pole. From 8−7.6 ka, the negative anomalies in the western pole become more negative, the $17^{o}C$ isotherm moves up again and the dipole becomes negative (Fig. 5d). Finally, after 7.6 ka, the isotherms slowly deepen again, driving the SASD to be positive again.

A comparison of the wind-driven isothermal shift from the 1.5 layer model with the $17^{o}C$ depth shift obtained from the simulations illustrates how the wind effect changes the thermocline. To simplify the text here, we will call the depth of the $17^{o}C$ isotherm obtained directly in the water column of each simulation Z17. This parameter differs from the wind-driven one calculated from the 1.5 layer model. The changes in the depth of Z17 in TrACE, UVic and CCSM3 show a deepening when freshwater forcing is added to the North Atlantic (9−8 ka, Fig 7a; c, years 1−100, Fig. 7b). Deepening in all the models seems to be concentrated within the South Atlantic eastern boundary. At $20^{o}W$ in TrACE, the Z17 deepens by up to 15 m, while in the CCSM3 and UVic, it deepens by 15 m and 30 m, respectively. The South Atlantic temperature increase is expected in a slowing overturning scenario due to slow northward heat transport. As the bipolar seesaw shifts towards a state of slower northward heat transport, heat concentrates in the South Atlantic (Pedro et al., 2018). Thus, the isothermal deepening results are consistent with the bipolar seesaw variability. However, as the AMOC slows down, the winds over the South Atlantic in the simulations cause a shallowing of the isotherms, mostly in the western South Atlantic (Fig. 7d−f). This shallowing and the heat addition to the South Atlantic creates the final pattern of deeper eastern isotherms and warms up the surface of the northeast pole. A warmer northeast South Atlantic then reduces the SASD index.

After the meltwater forcing period ends (after 8 ka and year 100), the TrACE Z17 moves up again, with stronger shallowing in the eastern Atlantic (8−7.5 ka), which induces a positive shift in the

Fig. 7. Mean depth anomaly (m) of the $17^{o}C$ isotherm from $15^{o}S$ to $40^{o}S$. a, b and c are the simulated anomalies, and d, e and f are the wind predicted anomalies ($h(x, y)$) for the TrACE, CCSM3 and UVic experiments, respectively. Dashed and dotted boxes show the values within the longitude ranges of the northeast and southwest SASD poles.

SASD. This vertical displacement in Z17 is not evident in the CCSM3 simulation, but it can be seen in the UVic results. The absence of uplift in Z17 in the CCSM3 simulation does not necessarily discredit the SASD return to positive values. Especially because other oceanic signals, such as water mass entrance or wave propagation, interfere with the measured isothermal displacement. The dynamic analysis shows that South Atlantic winds push the western isotherms upwards, while ocean dynamics heat up the surface of the South Atlantic. The combination of these two factors act by concentrating heat in the eastern South Atlantic and pushing the SASD towards negative values. It is important to highlight that there is a difference in the magnitude of the vertical migration of the Z17 and the wind-driven isothermal deepening. That is because the 1.5 layer model does not simulate the propagation of eastern boundary isothermal deepening into the interior ocean by Rossby waves. Hence, it is likely that other processes triggered by freshwater addition in the North Atlantic amplify the isothermal deepening in eastern South Atlantic.

Finally, none of the previously analyzed signals seem to have a large response by 8.5 ka or year 1; i.e., they do not seem to be directly forced by the lake outburst, showing that background slow freshwater addition is more important for modulating the SASD than abrupt freshwater release.

8. Wind anomalies between AMOC states

The 1.5 layer analysis suggests that wind anomalies during different AMOC states shift the zonal heat distribution, hence shifting the SASD state. Here, we will investigate the SST and wind patterns under the AMOC slowdown and recovery states. Meridional (zonal) winds control zonal (meridional) surface transport; hence, we will use the wind components to understand the transport of surface waters. It is important to highlight however that changes in the meridional winds affect mostly the eastern boundary isotherms, while its propagation to internal ocean happens due to Rossby waves propagation.

Trade winds in the TrACE experiment weakened during the AMOC slowdown phase, while the anomalies in the westerly winds seemed to vary with longitude (Figs. 8,9-8 ka). During the AMOC slowdown phase, the SSTs increased by 0.2^oC in the northeast South Atlantic, while the southwest South Atlantic cooled. Weakening of the meridional winds can decrease westward Ekman transport and hence concentrate heat in the eastern South Atlantic. Additionally, weakening of the trade wind's zonal component can concentrate warm surface waters in the northern South Atlantic. In fact, the time series of the meridional component of the trade winds between 0 and 20^oS show a 0.1 m/s weakening, while the zonal component weakens by 0.2 m/s from 9-8 ka. After 8 ka, the trade wind speeds increase. The westerlies, however, do not seem to have any measurable signal through the whole simulation, hence not necessarily affecting the SASD signal. SST anomalies agree with a negative SASD phase from 9 to 8 ka. In the AMOC recovery phase, the wind anomalies decrease, and the SST anomalies between poles revert, agreeing with a positive SASD phase.

In CCSM3, while the AMOC weakens in the first 100 years of simulation, the meridional (zonal) component of the trade winds weakens by 0.3 m/s (0.6 m/s), and positive SST anomalies appear in the northeast South Atlantic (Fig. 9). SST anomalies in this phase also point to a negative SASD. The westerlies do not show any apparent trend throughout the simulation. In the AMOC return phase, the SST anomalies revert, with cooling in the northeast pole and warming in the southwest pole. At this point, wind anomalies show that the trade winds strengthen again.

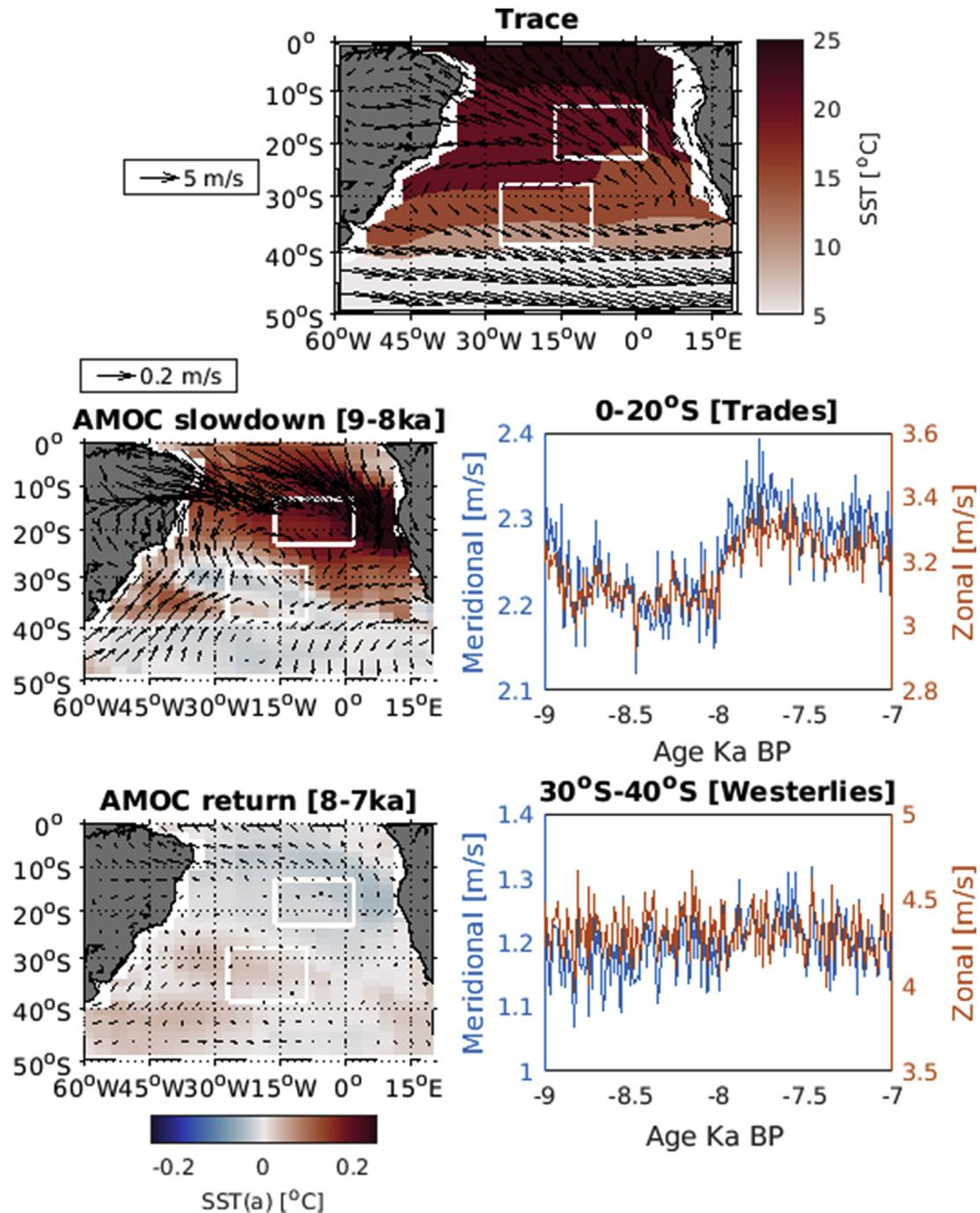The UVic simulation wind anomaly maps and time series show that the meridional component of the trade winds also weakens by 0.04m/s, and the zonal component weakens by 0.02m/s during the AMOC slowdown phase (Fig. 10, 9-8.2 ka). In contrast to previous simulations, the westerlies seem to accelerate in the UVic simulation by 0.03m/s from 9-8 ka. The SST anomalies show a warming phenomenon concentrated in the northeast pole, also pointing to a negative SASD. After 8 ka, while the AMOC accelerates, the mean meridional component of the trade winds increases again, and the northeast pole cools down. The signal of the westerlies after 8 ka seems to have a response identical to the bipolar seesaw EOF (Fig. 5c).

9. Summary and conclusions

The SAMS is one of the most important modes of precipitation variability in South America (Vera et al., 2006). Specifically, an early-Holocene SAMS intensification has been proposed (Wainer et al., 2014), most likely connected to meltwater fluxes into the North Atlantic. This points to the initial question raised in the introduction: (1) Does the spatial pattern of reconstructed South American precipitation points to a strengthening of the SAMS around 9-8 ka? We indeed found this phenomenon. The agreement and weakening of the $\delta^{18}O_p$ negative trends towards southern South America (Section 3) corroborates that hypothesis. Cheng et al. (2009) present evidence of a precipitation increase in South America connected to the 8.2 ka event. Although our study agrees with their findings, we advise caution since there are still too few speleothem records in South America that can be analyzed to infer the SAMS signal for the study period.

The study of other analogous periods with weakening overturning can provide evidence of the validity of the early-Holocene changes proposed here. The examination of widespread continental precipitation records by Stríkis et al. (2011) shows evidence of increased SAMS during 8.2 ka. Additionally, an intense strengthening of the SAMS has been proposed for Heinrich Stadials 1a and 1c (Stríkis et al., 2015). Heinrich events are associated with ice rafting, weakened overturning and the southward migration of the Intertropical Convergence Zone (Broecker et al., 1992), all processes used to explain our proposed SAMS strengthening mechanism. We conclude that the documented SAMS intensification regimes during other low-overturning states corroborate our hypothesis of a stronger SAMS due to meltwater addition to the North Atlantic during the 8.2 ka event.

Modeling experiments with AMOC weakening in the North Atlantic have shown an increase in South American precipitation and a change in the South Atlantic heat distribution (Frierson et al., 2013; Mulitza et al., 2017). Wainer et al. (2014) proposed that South Atlantic surface heat variability plays a key role in early-Holocene SAMS intensification, specifically due to the SASD teleconnection. However, is the SASD-SAMS shift caused by freshwater addition to the North Atlantic (2)? Our results indicate that it is. Simulations in which the single transient forcing is the meltwater addition to the North Atlantic reproduce SASD shifts similar in magnitude to the reconstructions. While we used two different models and three simulations in this study, this mechanism will need to be tested with other models. Furthermore, other transient forcings could also contribute to the SASD signal. The rising atmospheric temperatures in the early Holocene might play a role by causing widespread warming of the South Atlantic and increased South Atlantic evaporation. However, freshwater-triggered trade wind weakening is most likely the direct contributor to SASD-SAMS changes. Further sensitivity studies with a variety of single-forcing experiments are required to quantify the effect of each climate component on the strengthening of the SAMS. Additionally, Lopez et al. (2016) suggested that decadal variations in AMOC and the Atlantic meridional heat transport can be potential predictors of the strength of the
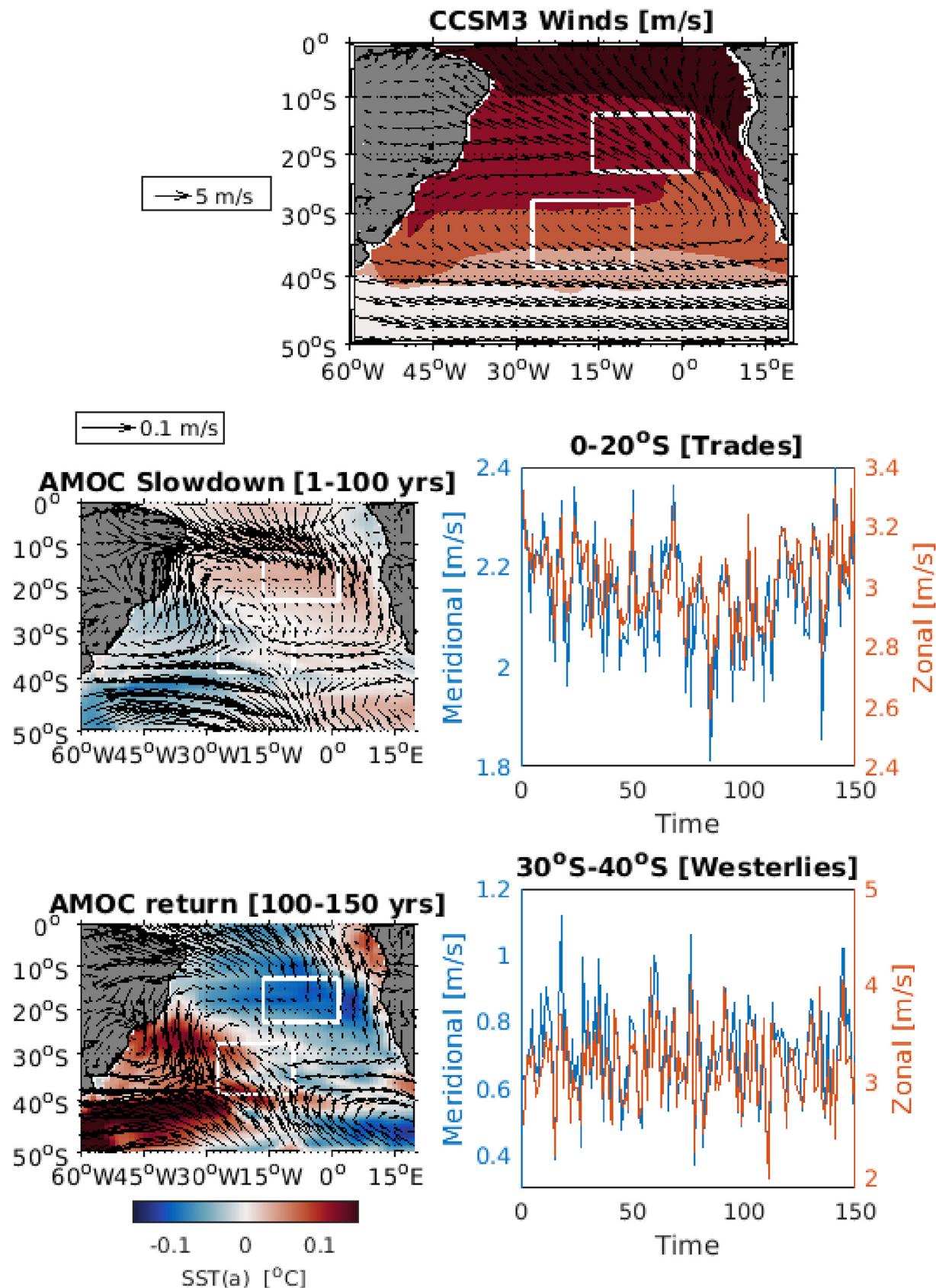
Fig. 8. Wind anomalies during the AMOC slowdown (9–8 ka) and AMOC recovery phases (8–7 ka) in TrACE. The map colors are the SST anomalies, and the time series show that the mean surface wind components within the Atlantic. Anomalies are calculated using the 9–7 ka mean. White boxes show the location of the northeast and southwest SASD poles. (For interpretation of the references to color in this figure legend, the reader is referred to the Web version of this article.)
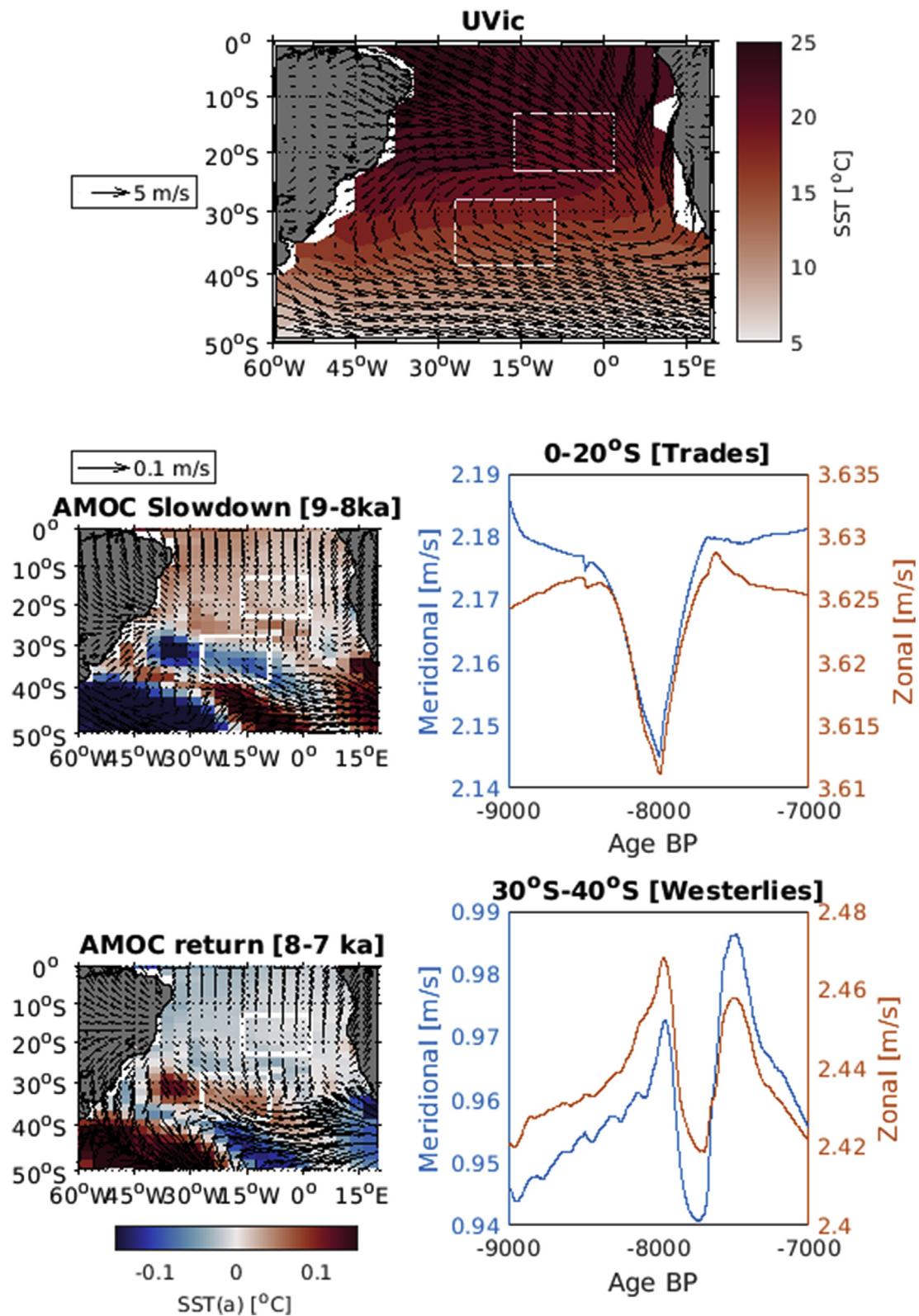
global monsoons within a 20 years adjustment lag. Indeed, in our analysis, we find evidence that a weakening of AMOC and the consequent anomalies in South Atlantic SSTs during the early-Holocene can enhance the South American Monsoonal system.

Finally, (3) what are the mechanisms causing the negative SASD and strengthened SAMS during the early Holocene? Here, the proposed mechanism is based on ocean and atmospheric changes during the low-overturning phase: As the AMOC slows down, heat concentrates in the South Atlantic and the trade winds in Southern Hemisphere weaken. Weakened trade winds push the isotherms

upwards, with higher vertical movement on the western South Atlantic. This differential isothermal uplift contributes to more heat being stored in the eastern South Atlantic, warming up the northeast SASD pole. Warmer waters in the northeast South Atlantic enhance evaporation. Excess moisture is then transported to northeast South America, where the SAMS regime is then intensified. Freshwater forcing has been identified as one of the trigger mechanisms for SAMS intensification (Stríkis et al., 2011). Caution has to be taken regarding the interpretation of our results for three reasons. First, the signal found here for the SASD-driven SAMS shift

Fig. 9. Wind anomalies during the AMOC slowdown (1−100 years) and resumption phases (100−150 years) in CCSM3. The map colors are the SST anomalies, and the time series represent the mean components within the Atlantic. The anomalies are calculated using the 1−150 year mean. (For interpretation of the references to color in this figure legend, the reader is referred to the Web version of this article.)

Fig. 10. Wind anomalies during the AMOC slowdown (9–8 ka) and AMOC resumption phases (8–7 ka) in the UVic model. The map colors are the SST anomalies, and the time series represent the mean wind components within the Atlantic. The anomalies are calculated using the 9–7 ka mean. (For interpretation of the references to color in this figure legend, the reader is referred to the Web version of this article.)

is likely embedded within a larger picture of South Atlantic warming. Widespread warming is the first South Atlantic signal in the SST when the AMOC slows down (Pedro et al., 2018). This warming increases South Atlantic evaporation, which likely leads to enhanced continental precipitation. The mechanism proposed here is a second-order SST signal regarding heat redistribution from the southwest to the northeast South Atlantic. In our simulations, this pattern explains up to 31% of the SST variance during the AMOC slowdown and up to 50% of the precipitation increase in the early Holocene. Second, SAMS intensification in low-overturning states has also been associated with the El Niño−Southern Oscillation variability by causing anomalies in the Walker cell circulation and triggering convective rain in northeastern South America (Ropelewski and Halpert, 1989). However, the influence of each of the processes is still under debate (Aceituno, 1988; Zhou and Lau, 2001; Kayano et al., 2013), and we consider the evaluation of the El Niño signal in Holocene precipitation out of the scope of the present study. Another feature of South American precipitation not analyzed here is the modulation of the zonal precipitation regime over the Amazon Basin. This modulation is most likely affected by changes in the SASD since negative SASD intensifies monsoons mostly in the eastern Brazil basin (Wainer et al., 2014). However, we consider this result to be an issue to be addressed in future studies. Third, present-day SASD events are connected to southward migration of the subtropical high and differential heat fluxes between the SASD poles (Morioka et al., 2011). Latent heat fluxes are mostly considered the main driver, although heat concentration due to zonal Ekman transport also contributes to differential pole SST anomalies (Sterl and Hazeleger, 2003). Our analysis shows that for the early Holocene, weakening of the trade winds changes the ocean vertical temperature structure, which together with extra South Atlantic heat due to the AMOC slowdown, changes the SASD index to negative values. The proposed mechanism explains how extra heating in the surface South Atlantic contributes to the SASD establishment and phase. One mechanism does not necessarily exclude the other; in fact, the weakening of the trade winds can be a consequence of subtropical high weakening. Future studies should evaluate the role of each one of the mechanisms in the establishment of negative SASD values.

Although high-resolution proxies that quantitatively measure precipitation are scarce in South America, several nonquantitative evidence of an increased SAMS exists. Rodrigues-Filho et al. (2002) found deposition of slope-wash sequences in Lake Silvana from 9.4 to 8 ka, suggesting rising lake levels and an extreme increase in rainfall. An analysis of vegetation changes in southeastern Brazil found increasing pollen counts from high-humidity species concurrent with the increase in the level of Lake Silvana during 9.5−8.6 ka BP (Pereira et al., 2012; Rodrigues et al., 2016). Lago do Pires pollen stratigraphy in Northeast Brazil records an increase in gallery forests and suggests an increase in precipitation from 8.8 to 7.5 ka BP (Behling, 1995). Other lake and cave reconstructions also point to increased precipitation during this early Holocene time span (Behling, 2003; Cheng et al., 2009; Horák-Terra et al., 2015).

Further modeling experiments to validate the proposed mechanism need to be performed, especially to test its validity during other meltwater events, such as the Younger Dryas, Heinrich events and Dansgaard-Oeschger events, and to evaluate the effect of solar and greenhouse gas forcing on the SAMS. Future studies with widespread speleothem reconstructions along South America and coastal SST reconstructions can also be used to test the validity of the SASD-SAMS signal in the early Holocene. Finally, the suggested ongoing AMOC weakening is likely a consequence of current global climate change. Changes in the SASD dipole and SAMS are already depicted in other studies (Liebmann et al., 2004; Hsu et al., 2012). Hence, future studies should analyze the coevolution of SASD and SAMS in future AMOC change scenarios.

Declaration of competing interest

The authors declare that they have no known competing financial interests or personal relationships that could have appeared to influence the work reported in this paper.

Acknowledgement

Appendix A. Supplementary data

Supplementary data to this article can be found online at https://doi.org/10.1016/j.quascirev.2020.106498.

Data availability

All the data used in this research is available by contact to the corresponding author and in the Zenodo database (https://doi.org/10.5281/zenodo.3975176)

Author contribution

The respective contribution of each author to the manuscript is listed below. The descriptions here depicted are accurate and agreed upon by all authors.

Wilton Aguiar: Conceptualization, Methodology, Software, Validation, Formal analysis, Investigation, Data curation, Writing - original draft, Writing - review & editing, Visualization. Luciana F. Prado: Conceptualization, Methodology, Software, Validation, Formal analysis, Investigation, Writing - review & editing, Visualization. Ilana Wainer: Conceptualization, Methodology, Validation, Formal analysis, Writing - review & editing, Visualization, Resources, Supervision. Zhengyu Liu: Conceptualization, Methodology, Validation, Formal analysis, Writing - review & editing, Visualization, Resources, Supervision. Alvaro Montenegro: Conceptualization, Methodology, Validation, Formal analysis, Writing - review & editing, Visualization, Resources, Supervision. Katrin J. Meissner: Conceptualization, Methodology, Validation, Formal analysis, Writing - review & editing, Visualization, Resources, Supervision. Mauricio M. Mata: Conceptualization, Methodology, Validation, Formal analysis, Writing - review & editing, Visualization, Resources, Supervision, Project administration, Funding acquisition.

References

Aceituno, P., 1988. On the functioning of the Southern Oscillation in the South American sector. Part I: surface climate. Mon. Weather Rev. 116, 505−524,

10.1175/1520-0493(1988)116<0505:OTFOTS>2.0.CO;2.

Aguiar, W., Mata, M., Kerr, R., 2017. On deep convection events and Antarctic Bottom Water formation in ocean reanalysis products. Ocean Sci. 13 https://doi.org/10.5194/os-13-851-2017.

Alley, R.B., Ágústsdóttir, A.M., 2005. The 8k event: cause and consequences of a major Holocene abrupt climate change. Quat. Sci. Rev. 24, 1123–1149. https://doi.org/10.1016/j.quascirev.2004.12.004. http://www.sciencedirect.com/science/article/pii/S0277379105000314.

Archer, D., 1996. A data-driven model of the global calcite lysocline. Global Biogeochem. Cycles 10, 511–526, 10.1029/96GB01521. https://agupubs.onlinelibrary.wiley.com/doi/abs/10.1029/96GB01521.

Azaneu, M., Kerr, R., Mata, M.M., 2014. Assessment of the representation of antarctic bottom water properties in the ECCO 2 reanalysis. Ocean Sci. https://doi.org/10.5194/os-10-923-2014.

Bagniewski, W., Meissner, K.J., Menviel, L., Brennan, C.E., 2015. Quantification of factors impacting seawater and calcite δ18O during Heinrich Stadials 1 and 4. Paleoceanography 30 895–911. https://doi.org/10.1002/2014PA002751, 10.1002/2014PA002751.

Bagniewski, W., Meissner, K.J., Menviel, L., 2017. Exploring the oxygen isotope fingerprint of Dansgaard-Oeschger variability and Heinrich events. Quat. Sci. Rev. 159, 1–14. https://doi.org/10.1016/j.quascirev.2017.01.007. http://www.sciencedirect.com/science/article/pii/S0277379117300203.

Bartlein, P.J., Harrison, S.P., Brewer, S., Connor, S., Davis, B.A.S., Gajewski, K., Guiot, J., Harrison-Prentice, T.I., Henderson, A., Peyron, O., Prentice, I.C., Scholze, M., Seppä, H., Shuman, B., Sugita, S., Thompson, R.S., Viau, A.E., Williams, J., Wu, H., 2011. Pollen-based continental climate reconstructions at 6 and 21Â ka: a global synthesis. Clim. Dynam. 37, 775–802. https://doi.org/10.1007/s00382-010-0904-1, 10.1007/s00382-010-0904-1.

Behling, H., 1995. Investigations into the late pleistocene and Holocene history of vegetation and climate in santa catarina (S Brazil). Veg. Hist. Archaeobotany. https://doi.org/10.1007/BF00203932.

Behling, H., 2003. Late glacial and Holocene vegetation, climate and fire history inferred from Lagoa Nova in the southeastern Brazilian lowland. Veg. Hist. Archaeobotany. https://doi.org/10.1007/s00334-003-0020-9.

Berger, A., 1978. Long-term variations of caloric insolation resulting from the earth's orbital elements. Quat. Res. 9, 139–167. https://doi.org/10.1016/0033-5894(78)90064-9. http://www.sciencedirect.com/science/article/pii/0033589478900649.

Bernal, J.P., Cruz, F.W., Stríkis, N.M., Wang, X., Deininger, M., Catunda, M.C.A., Ortega-Obregón, C., Cheng, H., Edwards, R.L., Auler, A.S., 2016. High-resolution Holocene south American monsoon history recorded by a speleothem from Botuverá cave, Brazil. Earth Planet Sci. Lett. 450, 186–196. https://doi.org/10.1016/j.epsl.2016.06.008. http://www.sciencedirect.com/science/article/pii/S0012821X16302953.

Boski, T., Bezerra, F.H.R., de Fátima Pereira, L., Souza, A.M., Maia, R.P., Lima-Filho, F.P., 2015. sea-level rise since 8.2ka recorded in the sediments of the Potengiâ€"Jundiai estuary, NE brasil. Mar. Geol. 365, 1–13. https://doi.org/10.1016/j.margeo.2015.04.003. http://www.sciencedirect.com/science/article/pii/S0025322715000869.

Brennan, C.E., Weaver, A.J., Eby, M., Meissner, K.J., 2012. Modelling oxygen isotopes in the university of Victoria earth system climate model for pre-industrial and last glacial maximum conditions. Atmos.-Ocean 50, 447–465. https://doi.org/10.1080/07055900.2012.707611, 10.1080/07055900.2012.707611.

Brennan, C.E., Meissner, K.J., Eby, M., Hillaire-Marcel, C., Weaver, A.J., 2013. Impact of sea ice variability on the oxygen isotope content of seawater under glacial and interglacial conditions. Paleoceanography. https://doi.org/10.1002/palo.20036.

Broecker, W.S., 1998. Paleocean circulation during the Last Deglaciation: a bipolar seesaw? Paleoceanography 13, 119–121. https://doi.org/10.1029/97PA03707, 10.1029/97PA03707.

Broecker, W., Bond, G., Klas, M., Clark, E., McManus, J., 1992. Origin of the northern Atlantic's Heinrich events. Clim. Dynam. https://doi.org/10.1007/BF00193540.

Carlson, A.E., Clark, P.U., Haley, B.A., Klinkhammer, G.P., 2009. Routing of western Canadian Plains runoff during the 8.2 ka cold event. Geophys. Res. Lett. 36, 10.1029/2009GL038778. https://agupubs.onlinelibrary.wiley.com/doi/abs/10.1029/2009GL038778.

Carvalho, L.M.V., Cavalcanti, I.F.A., 2016. the South American monsoon system. $10.1007/978-3-319-21650-8_6$.

Cavalcanti, I.F.A., 2012. Large scale and synoptic features associated with extreme precipitation over South America: a review and case studies for the first decade of the 21st century. Atmos. Res. 118, 27–40. https://doi.org/10.1016/j.atmosres.2012.06.012. http://www.sciencedirect.com/science/article/pii/S0169809512001871.

Cheng, H., Fleitmann, D., Edwards, R.L., Wang, X., Cruz, F.W., Auler, A.S., Mangini, A., Wang, Y., Kong, X., Burns, S.J., Matter, A., 2009. Timing and structure of the 8.2 kyr B.P. event inferred from δ18O records of stalagmites from China, Oman, and Brazil. Geology 37, 1007–1010. https://doi.org/10.1130/G30126A.1, 10.1130/G30126A.1.

Chiang, J.C.H., Bitz, C.M., 2005. Influence of high latitude ice cover on the marine Intertropical Convergence Zone. Clim. Dynam. 25, 477–496. https://doi.org/10.1007/s00382-005-0040-5, 10.1007/s00382-005-0040-5.

Chiang, J.C.H., Cheng, W., Bitz, C.M., 2008. Fast teleconnections to the tropical Atlantic sector from Atlantic thermohaline adjustment. Geophys. Res. Lett. 35 https://doi.org/10.1029/2008GL033292, 10.1029/2008GL033292.

Clark, P.U., Mix, A.C., 2002. Ice sheets and sea level of the last glacial maximum. Quat. Sci. Rev. 21, 1–7. https://doi.org/10.1016/S0277-3791(01)00118-4. http://

www.sciencedirect.com/science/article/pii/S0277379101001184.

Clarke, G.K.C., Leverington, D.W., Teller, J.T., Dyke, A.S., 2004. Paleohydraulics of the last outburst flood from glacial Lake Agassiz and the 8200BP cold event. Quat. Sci. Rev. 23, 389–407.

dos Santos-Fischer, C.B., Weschenfelder, J., Corrêa, I.C.S., Stone, J.R., Dehnhardt, B.A., Bortolin, E.C., 2018. A drowned lagunar channel in the southern Brazilian coast in response to the 8.2-ka event: diatom and seismic stratigraphy. Estuar. Coast 41, 1601–1625. https://doi.org/10.1007/s12237-018-0373-z, doi:10.1007/s12237-018-0373-z.

Ellison, C.R.W., Chapman, M.R., Hall, I.R., 2006. Surface and deep ocean interactions during the cold climate event 8200 Years ago. LP − 1932 Science 312, 1929, 10.1126/science.1127213. http://science.sciencemag.org/content/312/5782/1929.abstract.

Farmer, E.C., DeMenocal, P.B., Marchitto, T.M., 2005. Holocene and deglacial ocean temperature variability in the Benguela upwelling region: implications for low-latitude atmospheric circulation. Paleoceanography 20, 10.1029/2004PA001049. https://agupubs.onlinelibrary.wiley.com/doi/abs/10.1029/2004PA001049.

Frierson, D.M., Hwang, Y.T., Fučkar, N.S., Seager, R., Kang, S.M., Donohoe, A., Maroon, E.A., Liu, X., Battisti, D.S., 2013. Contribution of ocean overturning circulation to tropical rainfall peak in the Northern Hemisphere. Nat. Geosci. https://doi.org/10.1038/ngeo1987.

Garcia, S., Kayano, M., 2010. Some evidence on the relationship between the South American monsoon and the Atlantic ITCZ. Theor. Appl. Climatol. https://doi.org/10.1007/s00704-009-0107-z.

Gregoire, L.J., Payne, A.J., Valdes, P.J., 2012. Deglacial rapid sea level rises caused by ice-sheet saddle collapses. Nature 487, 219. https://doi.org/10.1038/nature11257. https://www.nature.com/articles/nature11257.

Hall, I.R., Bianchi, G.G., Evans, J.R., 2004. Centennial to millennial scale Holocene climate-deep water linkage in the North Atlantic. Quat. Sci. Rev. 23, 1529–1536.

He, F., 2011. Simulating Transient Climate Evolution of the Last Deglaciation with CCSM3.

Hibler, W.D., 1979. A dynamic thermodynamic sea ice model. J. Phys. Oceanogr. 9, 815–846. https://doi.org/10.1175/1520-0485(1979)009<0815:ADTSIM>2.0.CO;2.

Horák-Terra, I., Martínez Cortizas, A., da Luz, C.F.P., Rivas López, P., Silva, A.C., Vidal-Torrado, P., 2015. Holocene climate change in central-eastern Brazil reconstructed using pollen and geochemical records of Pau de Fruta mire (Serra do Espinhaço Meridional, Minas Gerais). Palaeogeogr. Palaeoclimatol. Palaeoecol. https://doi.org/10.1016/j.palaeo.2015.07.027.

Hsu, P.C., Li, T., Luo, J.J., Murakami, H., Kitoh, A., Zhao, M., 2012. Increase of global monsoon area and precipitation under global warming: a robust signal? Geophys. Res. Lett. https://doi.org/10.1029/2012GL051037.

Jansen, E., Andersson, C., Moros, M., Nisancioglu, K.H., Nyland, B.F., Telford, R.J., 2008. The early to mid-holocene thermal optimum in the north atlantic, 10.1002/9781444300932.ch5. https://doi.org/10.1002/9781444300932.ch5.

Joos, F., Spahni, R., 2008. Rates of change in natural and anthropogenic radiative forcing over the past 20,000 years. Proc. Natl. Acad. Sci. Unit. States Am. 105, 1425–1430, 10.1073/pnas.0707386105. https://www.pnas.org/content/105/5/1425.

Kalnay, E., Kanamitsu, M., Kistler, R., Collins, W., Deaven, D., Gandin, L., Iredell, M., Saha, S., White, G., Woollen, J., Zhu, Y., Leetmaa, A., Reynolds, R., Chelliah, M., Ebisuzaki, W., Higgins, W., Janowiak, J., Mo, K.C., Ropelewski, C., Wang, J., Jenne, R., Joseph, D., 1996. The NCEP/NCAR 40-year reanalysis Project. Bull. Am. Meteorol. Soc. 77, 437–471. https://doi.org/10.1175/1520-0477(1996)077<0437:TNYRP/E2.0.CO.

Kaufman, D.S., Ager, T.A., Anderson, N.J., Anderson, P.M., Andrews, J.T., Bartlein, P.J., Brubaker, L.B., Coats, L.L., Cwynar, L.C., Duvall, M.L., 2004. Holocene thermal maximum in the western Arctic (0180 W). Quat. Sci. Rev. 23, 529–560.

Kayano, M.T., Andreoli, R.V., Ferreira de Souza, R.A., 2013. Relations between ENSO and the South Atlantic SST modes and their effects on the South American rainfall. Int. J. Climatol. 33, 2008–2023. https://doi.org/10.1002/joc.3569, 10.1002/joc.3569.

Kim, J.H., Schneider, R.R., Müller, P.J., Wefer, G., 2002. Interhemispheric comparison of deglacial sea-surface temperature patterns in Atlantic eastern boundary currents. Earth Planet Sci. Lett. https://doi.org/10.1016/S0012-821X(01)00545-3.

Kim, J.H., Schneider, R.R., Mulitza, S., Müller, P.J., 2003. Reconstruction of SE trade-wind intensity based on sea-surface temperature gradients in the Southeast Atlantic over the last 25 kyr. Geophys. Res. Lett. https://doi.org/10.1029/2003GL017557.

Kleiven, H.K.F., Kissel, C., Laj, C., Ninnemann, U.S., Richter, T.O., Cortijo, E., 2008. Reduced North Atlantic deep water coeval with the glacial Lake Agassiz freshwater outburst. Science 319, 60. LP − 64. http://science.sciencemag.org/content/319/5859/60.abstract.

Kodama, Y., 1992. Large-scale common features of subtropical precipitation zones, part I: characteristics of subtropical frontal zones. J. Meteorol. Soc. Jpn. https://doi.org/10.2151/jmsj1965.70.4813.

Liebmann, B., Mechoso, C.R., 2011. The global monsoon system: research and forecast. South American monsoon system. World Scientific. https://doi.org/10.1142/9789814343411_0009.

Liebmann, B., Vera, C.S., Carvalho, L.M., Camilloni, I.A., Hoerling, M.P., Allured, D., Barros, V.R., Báez, J., Bidegain, M., 2004. An observed trend in central South American precipitation. J. Clim. https://doi.org/10.1175/3205.1.

Lopez, H., Dong, S., Lee, S.K., Goni, G., 2016. Decadal modulations of interhemispheric global atmospheric circulations and monsoons by the south atlantic

meridional overturning circulation. J. Clim. 29, 1831–1851. https://doi.org/10.1175/JCLI-D-15-0491.1, 10.1175/JCLI-D-15-0491.1.

Lorenz, E.N., 1956. Empirical Orthogonal Functions and Statistical Weather Prediction.

Meissner, K.J., Weaver, A.J., Matthews, H.D., Cox, P.M., 2003. The role of land surface dynamics in glacial inception: a study with the UVic Earth System Model. Clim. Dynam. 21, 515–537. https://doi.org/10.1007/s00382-003-0352-2, 10.1007/s00382-003-0352-2.

Meissner, K.J., Eby, M., Weaver, A.J., Saenko, O.A., 2007. CO2 threshold for millennial-scale oscillations in the climate system: implications for global warming scenarios. Clim. Dynam. 30, 161. https://doi.org/10.1007/s00382-007-0279-0, 10.1007/s00382-007-0279-0.

Monerie, P.A., Robson, J., Dong, B., Hodson, D.L.R., Klingaman, N.P., 2019. Effect of the Atlantic multidecadal variability on the global monsoon. Geophys. Res. Lett. https://doi.org/10.1029/2018GL080903.

Morioka, Y., Tozuka, T., Yamagata, T., 2011. On the growth and decay of the subtropical dipole mode in the south atlantic. J. Clim. 24, 5538–5554. https://doi.org/10.1175/2011JCLI4010.1, 10.1175/2011JCLI4010.1.

Morrill, C., Jacobsen, R.M., 2005. How widespread were climate anomalies 8200 years ago? n/a–-n/a Geophys. Res. Lett. 32. https://doi.org/10.1029/2005GL023536, 10.1029/2005GL023536.

Morrill, C., Anderson, D.M., Bauer, B.A., Buckner, R., Gille, E.P., Gross, W.S., Hartman, M., Shah, A., 2013. Proxy benchmarks for intercomparison of 8.2 ka simulations. Clim. Past 9, 423–432, 10.5194/cp-9-423-2013. http://www.clim-past.net/9/423/2013/.

Morrill, C., Ward, E.M., Wagner, A.J., Otto-Bliesner, B.L., Rosenbloom, N., 2014. Large sensitivity to freshwater forcing location in 8.2 ka simulations. Paleoceanography 29, 930–945. https://doi.org/10.1002/2014PA002669, 10.1002/2014PA002669.

Mulitza, S., Chiessi, C.M., Schefuß, E., Lippold, J., Wichmann, D., Antz, B., Mackensen, A., Paul, A., Prange, M., Rehfeld, K., Werner, M., Bickert, T., Frank, N., Kuhnert, H., Lynch-Stieglitz, J., Portilho-Ramos, R.C., Sawakuchi, A.O., Schulz, M., Schwenk, T., Tiedemann, R., Vahlenkamp, M., Zhang, Y., 2017. Synchronous and proportional deglacial changes in Atlantic meridional overturning and northeast Brazilian precipitation. Paleoceanography. https://doi.org/10.1002/2017PA003084.

Nieto-Ferreira, R., Rickenbach, T.M., 2011. Regionality of monsoon onset in South America: a three-stage conceptual model. Int. J. Climatol. https://doi.org/10.1002/joc.2161.

Nnamchi, H.C., Kucharski, F., Keenlyside, N.S., Farneti, R., 2017. Analogous seasonal evolution of the South Atlantic SST dipole indices. Atmos. Sci. Lett. https://doi.org/10.1002/asl.781.

Nogués-Paegle, J., Mo, K.C., 1997. Alternating wet and dry conditions over South America during summer. Mon. Weather Rev. 125, 279–291. https://doi.org/10.1175/1520-0493(1997)125{\}3C0279:AWADCO{\}3E2.0.CO, 10.1175/1520-0493(1997)125<0279:AWADCO>2.0.CO;2.

Novello, V.F., Cruz, F.W., Vuille, M., Stríkis, N.M., Edwards, R.L., Cheng, H., Emerick, S., De Paula, M.S., Li, X., Barreto, E.D.S., Karmann, I., Santos, R.V., 2017. A high-resolution history of the south American monsoon from last glacial maximum to the Holocene. Sci. Rep. https://doi.org/10.1038/srep44267.

Oppo, D.W., McManus, J.F., Cullen, J.L., 2003. Deepwater variability in the Holocene epoch. Nature 422, 277. https://doi.org/10.1038/422277b, 10.1038/422277b.

Otto-Bliesner, B.L., Brady, E.C., Clauzet, G., Tomas, R., Levis, S., Kothavala, Z., 2006. Last glacial maximum and Holocene climate in CCSM3. J. Clim. 19, 2526–2544. https://doi.org/10.1175/JCLI3748.1, 10.1175/JCLI3748.1.

Pacanowski, R.C., 1996. Documentation user's guide and reference manual (MOM2, Version 2). GFDL Ocean Technical Report 3, 329.

Pedro, J.B., Jochum, M., Buizert, C., He, F., Barker, S., Rasmussen, S.O., 2018. Beyond the bipolar seesaw: toward a process understanding of interhemispheric coupling. Quat. Sci. Rev. 192, 27–46, 10.1016/J.QUASCIREV.2018.05.005. https://www.sciencedirect.com/science/article/pii/S0277379117310351.

Peltier, W.R., 2004. Global glacial isostasy and the surface OF the ice-age earth: the ICE-5G (VM2) model and grace. Annu. Rev. Earth Planet Sci. 32, 111–149. https://doi.org/10.1146/annurev.earth.32.082503.144359, 10.1146/annurev.earth.32.082503.144359.

Pereira, N.V., Safford, H.D., Behling, H., 2012. Holocene vegetation and fire history of the Serra do Caparaó, SE Brazil. Holocene 22, 1243–1250. https://doi.org/10.1177/0959683612437864, 10.1177/0959683612437864.

Pivel, M.A.G., Santarosa, A.C.A., Toledo, F.A.L., Costa, K.B., 2013. The Holocene onset in the southwestern South atlantic. Palaeogeogr. Palaeoclimatol. Palaeoecol. 374, 164–172. https://doi.org/10.1016/j.palaeo.2013.01.014. http://www.sciencedirect.com/science/article/pii/S0031018213000357.

Pottapinjara, V., Girishkumar, M., Murtugudde, R., Ashok, K., R, M., 2019. On the relation between the boreal spring position of the atlantic intertropical convergence Zone and atlantic zonal mode. J. Clim. https://doi.org/10.1175/JCLI-D-18-0614.1.

Rodrigues, J.M., Behling, H., Giesecke, T., 2016. Holocene dynamics of vegetation change in southern and southeastern Brazil is consistent with climate forcing. Quat. Sci. Rev. 146, 54–65. https://doi.org/10.1016/j.quascirev.2016.06.011. http://www.sciencedirect.com/science/article/pii/S0277379116302116.

Rodrigues-Filho, S., Behling, H., Irion, G., Müller, G., 2002. Evidence for lake formation as a response to an inferred Holocene climatic transition in Brazil. Quat. Res. 57, 131–137. https://doi.org/10.1006/qres.2001.2281. http://www.sciencedirect.com/science/article/pii/S0033589401922811.

Ropelewski, C.F., Halpert, M.S., 1989. Precipitation patterns associated with the high index phase of the southern oscillation. J. Clim. https://doi.org/10.1175/1520-0442(1989)002<0268:ppawth>2.0.co;2.

Souza, P., Cavalcanti, I., 2009. Atmospheric centres of action associated with the Atlantic ITCZ position. Int. J. Climatol. https://doi.org/10.1002/joc.1823.

Sterl, A., Hazeleger, W., 2003. Coupled variability and air-sea interaction in the south atlantic ocean. Clim. Dynam. https://doi.org/10.1007/s00382-003-0348-y.

Stocker, T.F., Mysak, L.A., Wright, D.G., 1992. A zonally averaged, coupled ocean-atmosphere model for paleoclimate studies. J. Clim. https://doi.org/10.1175/1520-0442(1992)005<0773:AZACOA>2.0.CO;2.

Stríkis, N.M., Cruz, F.W., Cheng, H., Karmann, I., Edwards, R.L., Vuille, M., Wang, X., de Paula, M.S., Novello, V.F., Auler, A.S., 2011. Abrupt variations in South American monsoon rainfall during the Holocene based on a speleothem record from central-eastern Brazil. Geology 39, 1075–1078. https://doi.org/10.1130/G32098.1, 10.1130/G32098.1.

Stríkis, N.M., Chiessi, C.M., Cruz, F.W., Vuille, M., Cheng, H., De Souza Barreto, E.A., Mollenhauer, G., Kasten, S., Karmann, I., Edwards, R.L., Bernal, J.P., Sales, H.D.R., 2015. Timing and structure of mega-SACZ events during Heinrich stadial 1. Geophys. Res. Lett. https://doi.org/10.1002/2015GL064048.

Toledo, F., 2008. Tracing past circulation changes in the western South Atlantic based on planktonic foraminifera. Rev. Bras. Palaontol. https://doi.org/10.4072/rbp.2008.3.03.

Venegas, S.A., Mysak, L.A., Straub, D.N., 1996. Evidence for interannual and inter-decadal climate variability in the South Atlantic. Geophys. Res. Lett. https://doi.org/10.1029/96GL02373.

Venegas, S.A., Mysak, L.A., Straub, D.N., 1997. Atmosphere-ocean coupled variability in the south atlantic. J. Clim. https://doi.org/10.1175/1520-0442(1997)010<2904:AOCVIT>2.0.CO;2.

Vera, C., Higgins, W., Amador, J., Ambrizzi, T., Garreaud, R., Gochis, D., Gutzler, D., Lettenmaier, D., Marengo, J., Mechoso, C.R., Nogues-Paegle, J., Silva Dias, P.L., Zhang, C., 2006. Toward a Unified View of the American Monsoon Systems. https://doi.org/10.1175/JCLI3896.1.

Voarintsoa, N.R.G., Matero, I.S.O., Railsback, L.B., Gregoire, L.J., Tindall, J., Sime, L., Cheng, H., Edwards, R.L., Brook, G.A., Kathayat, G., Li, X., Michel Rakotondrazafy, A.F., Madison Razanatseheno, M.O., 2019. Investigating the 8.2 ka event in northwestern Madagascar: insight from dataâ€"model comparisons. Quat. Sci. Rev. 204, 172–186. https://doi.org/10.1016/j.quascirev.2018.11.030. http://www.sciencedirect.com/science/article/pii/S027737911830355X.

Wagner, R.G., 1996. Decadal-scale trends in mechanisms controlling meridional sea surface temperature gradients in the tropical Atlantic. J. Geophys. Res.: Oceans. https://doi.org/10.1029/96JC01214.

Wagner, A.J., Morrill, C., Otto-Bliesner, B.L., Rosenbloom, N., Watkins, K.R., 2013. Model support for forcing of the 8.2Å ka event by meltwater from the Hudson Bay ice dome. Clim. Dynam. 41, 2855–2873. https://doi.org/10.1007/s00382-013-1706-z, doi:10.1007/s00382-013-1706-z.

Wainer, I., Prado, L.F., Khodri, M., Otto-Bliesner, B., 2014. Reconstruction of the South Atlantic Subtropical Dipole index for the past 12,000 years from surface temperature proxy. Sci. Rep. 4, 5291. https://doi.org/10.1038/srep05291.

Walker, M.J.C., Berkelhammer, M., Björck, S., Cwynar, L.C., Fisher, D.A., Long, A.J., Lowe, J.J., Newnham, R.M., Rasmussen, S.O., Weiss, H., 2012. Formal subdivision of the Holocene series/epoch: a discussion paper by a working Group of INTI-MATE (integration of ice-core, marine and terrestrial records) and the sub-commission on quaternary stratigraphy (international commission on stratigraphy). J. Quat. Sci. 27, 649–659. https://doi.org/10.1002/jqs.2565, 10.1002/jqs.2565.

Walker, M., Head, M.J., Berkelhammer, M., Björck, S., Cheng, H., Cwynar, L., Fisher, D., Gkinis, V., Long, A., Lowe, J., Newnham, R., Rasmussen, S.O., Weiss, H., 2018. Formal ratification of the subdivision of the Holocene series/epoch (quaternary system/period): two new global boundary stratotype sections and points (GSSPs) and three new stages/subseries. Episodes. https://doi.org/10.18814/epiiugs/2018/018016.

Weaver, A.J., Eby, M., Wiebe, E.C., Bitz, C.M., Duffy, P.B., Ewen, T.L., Fanning, A.F., Holland, M.M., MacFadyen, A., Matthews, H.D., Meissner, K.J., Saenko, O., Schmittner, A., Wang, H., Yoshimori, M., 2001. The UVic earth system climate model: model description, climatology, and applications to past, present and future climates. Atmos.-Ocean 39, 361–428. https://doi.org/10.1080/07055900.2001.9649686, 10.1080/07055900.2001.9649686.

Yang, H., Zhao, Y., Liu, Z., Li, Q., He, F., Zhang, Q., 2015. Heat Transport Compensation in Atmosphere and Ocean over the Past 22 , 000 Years. Nature Publishing Group, pp. 1–11. https://doi.org/10.1038/srep16661, 10.1038/srep.16661.

Zhou, J., Lau, K.M., 2001. Principal modes of interannual and decadal variability of summer rainfall over South America. Int. J. Climatol. https://doi.org/10.1002/joc.700.

Zilli, M., Carvalho, L., Lintner, B., 2019. The poleward shift of South Atlantic Convergence Zone in recent decades. Clim. Dynam. https://doi.org/10.1007/s00382-018-4277-1.